Contrib Mineral Petrol (2009) 157:541–558
DOI 10.1007/s00410-008-0351-8

ORIGINAL PAPER

Igneous garnet and amphibole fractionation in the roots of island arcs: experimental constraints on andesitic liquids

Raquel Alonso-Perez · Othmar Müntener · Peter Ulmer

Received: 23 January 2008 / Accepted: 6 October 2008 / Published online: 30 October 2008

Abstract To evaluate the role of garnet and amphibole fractionation at conditions relevant for the crystallization of magmas in the roots of island arcs, a series of experiments were performed on a synthetic andesite at conditions ranging from 0.8 to 1.2 GPa, 800–1,000°C and variable H_2O contents. At water undersaturated conditions and fO_2 established around QFM, garnet has a wide stability field. At 1.2 GPa garnet + amphibole are the high-temperature liquidus phases followed by plagioclase at lower temperature. Clinopyroxene reaches its maximal stability at H_2O-contents $\leq$9 wt% at 950°C and is replaced by amphibole at lower temperature. The slopes of the plagioclase-in boundaries are moderately negative in T-X_{H_2O} space. At 0.8 GPa, garnet is stable at magmatic H_2O contents exceeding 8 wt% and is replaced by spinel at decreasing dissolved H_2O. The liquids formed by crystallization evolve through continuous silica increase from andesite to dacite and rhyolite for the 1.2 GPa series, but show substantial enrichment in FeO/MgO for the 0.8 GPa series related to the contrasting roles of garnet and amphibole in fractionating Fe–Mg in derivative liquids. Our experiments indicate that the stability of igneous garnet increases with increasing dissolved H_2O in silicate liquids and is thus likely to affect trace element compositions of H_2O-rich derivative arc volcanic rocks by fractionation. Garnet-controlled trace element ratios cannot be used as a proxy for 'slab melting', or dehydration melting in the deep arc. Garnet fractionation, either in the deep crust via formation of garnet gabbros, or in the upper mantle via formation of garnet pyroxenites remains an important alternative, despite the rare occurrence of magmatic garnet in volcanic rocks.

Keywords Experimental petrology · Hydrous andesite liquids · High-pressure crystallization · Amphibole · Garnet fractionation

Communicated by T. L. Grove.

R. Alonso-Perez · P. Ulmer
Institute of Mineralogy and Petrology, ETH, Zurich, Switzerland

O. Müntener (✉)
Institute of Mineralogy and Geochemistry,
University of Lausanne, Lausanne, Switzerland
e-mail: othmar.muntener@unil.ch

Introduction

Major and trace element similarities between estimates of the composition of the continental crust and calc-alkaline andesites indicate that subduction zones are one of the key areas in the generation of new continental crust (Gill 1981; Kay and Kay 1985; Kelemen et al. 2003; Rudnick 1995). A major question of continental crust formation is if and how fractionation of primary arc magmas could ultimately produce Si-rich derivative liquids that resemble the andesitic composition of continental crust (Taylor 1967). Major and trace element concentrations of volcanic and plutonic calc-alkaline differentiates in continental margin settings (e.g. Alps, Andes, Himalayas and Alaska) indicate that silica-poor minerals such as garnet, amphibole and Fe–Ti-oxides played a significant role during differentiation of basaltic liquids (Jan and Howie 1981; Ulmer et al. 1985; DeBari and Coleman 1989; Greene et al. 2006). Crystallization and fractionation of garnet at high pressure to generate high-silica calc-alkaline liquids has originally been proposed by Trevor Green and coworkers (Green 1972; Green and Ringwood 1968a, b), based on the occurrence of garnet-phenocrysts in calc-alkaline dacites

and on experimental phase equilibria on a series of calc-alkaline compositions (high-Al olivine tholeiite, high-Al qtz-tholeiite, basaltic andesite, andesite, dacite and rhyodacite). However, there is limited experimental data that have systematically investigated the influence of variable amounts of H_2O (and other volatiles) on the relative stabilities of garnet, amphibole, pyroxene and plagioclase in basaltic to andesitic liquids at conditions relevant for the lower arc crust (Green 1992; Müntener et al. 2001). Magmatic garnet has been described from andesitic to dacitic calc-alkaline volcanics (Day et al. 1992; Evans and Vance 1987; Fitton 1972; Harangi et al. 2001) indicating that high-pressure garnet crystallization and fractionation at a depth of 25–45 km is an important process in the generation of these lavas.

The potential localities and processes, where garnet might be involved in the petrogenesis of subduction-related magmas are schematically illustrated in Fig. 1. Four potential areas can be identified: (a) garnet fractionation at high pressure at the base of arc crust (Müntener and Ulmer 2006), (b) partial melting of mafic rocks at the base of arc crust, leaving a garnet-bearing granulitic residue (Atherton and Petford 1993), (c) partial melting of a garnet-lherzolite source (Ulmer 1989a) and melting of the subducted slab, leaving a rutile-bearing eclogite residue (Defant and Drummond 1990). Moreover, the occurrence of garnet-bearing ultramafic to mafic plutonic rocks in deep arc crustal sections and at the crust-mantle boundary (Kohistan arc, Pakistan: Burg et al. 1998; Jan and Howie 1981; Ringuette et al. 1999), south-central Alaskan Tonsina Complex (DeBari and Coleman 1989; Greene et al. 2006), as well as studies from crust and mantle xenoliths (Ducea and Saleeby 1996, 1998) provides compelling evidence that garnet fractionation/crystallization from basaltic magmas is a potentially important process in the differentiation of subduction-related magmas. The field observations that many of these terrains show cumulate

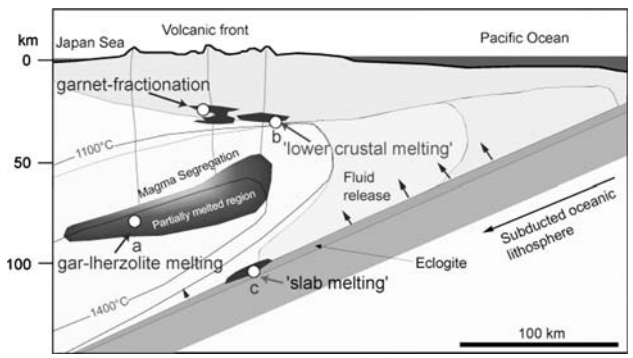

Fig. 1 Potential localities/processes where garnet could be involved in the genesis of andesitic magmas at convergent-plate margins (basic diagram modified after Kushiro 1987). Thin black lines are isotherms. See text for discussion

sequences support the important role of fractionation at high-pressure. The importance of amphibole fractionation in the genesis of calc-alkaline rocks was already proposed by Bowen (1928) and has been a hotly debated topic ever since (Allen et al. 1975; Cawthorn and O'Hara 1976; Green and Ringwood 1968b; Huang and Wyllie 1986; Sisson and Grove 1993a; Davidson et al. 2007). This debate has been revived in recent times, since detailed trace element partitioning studies advocate an important role of amphibole in fractionating geochemical 'twins', such as Nb and Ta (Blundy and Wood 2003; Tiepolo et al. 2000). The role of magnetite in the formation of calc-alkaline magmas was first discussed by Osborn (1959). He proposed that the lack of iron-enrichment in the calc-alkaline trend is caused by early fractionation of magnetite and is thus primarily controlled by oxygen fugacity. Clearly, differentiation of H_2O undersaturated magmas, under conditions relevant for the roots of island arc crust is a key for the understanding of the genesis of andesites and dacites, and thus for the continental crust in general.

Here, we present the results of a phase equilibria study on a H_2O-undersaturated andesitic composition in the temperature range of 800–1,000°C, pressures of 0.8–1.2 GPa, H_2O contents of 4, 6 and 8 wt% and fO_2 between ~QFM and Ni–NiO. We discuss the relative roles of garnet, amphibole, pyroxene and plagioclase on derivative, H_2O-undersaturated liquids in order to explore the effects of variable H_2O content on andesite phase equilibria under conditions relevant for arc crust formation. Finally, we will critically evaluate previous proposals invoking partial melting of the lower crust, or melting of the subducting slab (e.g. 'slab melting') as the dominant mechanisms in explaining geochemical peculiarities of subduction zone magmas.

Experimental design and analytical techniques

A synthetic andesite composition was used as starting material for this study (Table 1). The andesite composition was derived by a series of fractional crystallization experiments (Kägi 2000) conducted on a natural picrobasalt from the Adamello batholith, N-Italy (Ulmer 1986, 1989b). We remixed the derivative andesite from natural silicates, synthetic oxides and hydroxides in order to achieve variable H_2O contents, of about 4, 6 and 8 wt%. To constrain the redox conditions of the experiments close to the Ni–NiO buffer equilibrium, the "intrinsic" fO_2 approach was used (Kägi et al. 2005). The intrinsic fO_2 of the starting material was adjusted via the molar Fe_2O_3/FeO ratio of the starting powder by balancing Fe_2O_3 (hematite) and fayalite according to the equation of Kress and Carmichael (1991). We have chosen an initial value of

Table 1 Starting compositions used in this study

Starting material	SiO_2	TiO_2	Al_2O3	Fe_2O_3	FeO_{tot}	MnO	MgO	CaO	Na_2O	K_2O	H_2O	Total	Mg#
F8a-4	54.82	0.91	18.05	1.66	5.94	0.29	2.83	7.12	2.83	1.42	4.14	100	0.404
F8a-6	53.67	0.89	17.68	1.62	5.81	0.29	2.77	6.97	2.77	1.39	6.15	100	0.404
F8a-8	52.53	0.87	17.30	1.59	5.69	0.28	2.71	6.82	2.71	1.36	8.14	100	0.404

Starting compositions correspond to a liquid obtained by Kägi (2000) in fractional crystallization experiments starting from a hydrous picrobasalt at 1.0 GPa, 1020°C. Compositions were synthesized with 4, 6 and 8 wt% H_2O, respectively. Fe_2O_3 and FeO adjusted to a molar Fe_2O_3/FeO ratio of 0.125 corresponding to Ni–NiO + 0.6 at 1,000°C and 1.0 GPa according to Kress and Carmichael (1991). *Mg#* molar [MgO/(MgO + FeO)]; all Fe as Fe^{2+}. During a later phase of the study, new starting material was prepared, with identical major element composition, but with 2,000 μg/g trace elements added. These starting compositions are termed 4c, 6c and 8c in Table 2, respectively

0.125, corresponding to a log fO_2 of −9.35 (QFM + 1 or NNO + 0.6) at 1.0 GPa and 1,000°C. Firstly, SiO_2, TiO_2, MgO, $CaCO_3$ and Fe_2O_3 where weighed out and ground for 1 h (in order to obtain a grain size of ≤10 μm) under ethanol, using an agate mortar and pestle. The resulting powder was fired at 1,000°C for 2 h to decarbonate $CaCO_3$ and drive off adsorbed H_2O. This mixture was weighed after firing to determine whether the decarbonation of the $CaCO_3$ was complete. To this mixture, weighed aliquots of Fe_2SiO_4, Na_2SiO_3, $KAlSi_3O_8$, AlOOH, $Al(OH)_3$ and MnO were added in appropriate proportions, ground for 1 h under ethanol, using an agate mortar and pestle, and dried and stored at 110°C. Fayalite and K-feldspar were synthesized following the methods described by Kägi et al. (2005). No liquid H_2O was added to the starting material.

The experiments were carried out in end-loaded piston-cylinder apparatus using 14 mm diameter NaCl-Pyrex cells. The capsules were surrounded by alumina and Pyrex glass. A friction correction of −3% was applied. The temperature was measured using a type B $Pt_{94}Rh_6$, $Pt_{70}Rh_{30}$ thermocouple, with an estimated accuracy of ±5°; no corrections for the pressure effects on emf were applied. Switching off the power supply terminated the experiments and resulted in quench rates in the order of 100°C/s, which were high enough to quench the liquids to glass. Two different sets of experiments have been carried out: (1) Fe-presaturated 'sample-in-sample' double capsule technique and (2) double capsule technique. The double capsule technique was employed to minimize Fe-loss and H_2 diffusion and to constrain relatively high fO_2 (N–NNO + 1). In order to further minimize Fe-loss we pre-saturated the inner capsule ($Au_{90}Pd_{10}$ 2.3 mm outer diameter), which were filled with the identical starting material and held at 1 bar and 1,180°C in a vertical gas-mixing furnace for 48 h at an fO_2 of 1 log unit below the FMQ buffer (Gaetani and Grove 1998; Hall et al. 2004; Kägi et al. 2005). Tylan digital gas-flow controllers were used to control the CO_2–H_2 gas mixtures. After quenching, the capsules were cleaned in a warm HF bath for 48 h. After leaching, the cleaned Fe-presaturated capsule were filled with the appropriate starting materials, welded shut, and placed into the outer Pt capsule (4.0 mm outer diameter), which contained the same starting material. In some of the pre-saturated runs, especially those at high temperature, relative Fe-gain was observed (Table 2). Therefore, in subsequent experiments, we decided to use the double capsule technique without the pre-saturation procedure. Relative Fe losses or gains were always lower than 10% relative (estimates based on mass balance calculations) in all, but one case. Therefore, we assume that a relatively constant bulk composition was maintained during the experiments. H_2O loss during welding was avoided by freezing the capsule with liquid nitrogen and/or surrounding it with a wet tissue. Weight tests before and after welding indicated no loss of H_2O. Consequently, we are confident that a reasonable approach to closed-system conditions could be achieved in our experiments. Furthermore, we determined the H_2O content of the experimental glasses by Raman spectroscopy (Zajacz et al. 2005; Di Muro et al. 2006; Mercier et al. 2008), and compared these results with the theoretical H_2O-content calculated from the initial H_2O content and the fractions of liquid and amphibole through mass balance calculations (Table 2).

Our results (Table 2) show relatively large differences between calculated and measured H_2O contents, but with the exception of a few runs, the difference is <20%, which is acceptable, given the large uncertainties inherent in Raman spectroscopy (see below). We conclude that no significant H_2O loss has occurred in the reported experiments, with the exception of run rp43 (1.2 GPa, 900°C, 8 wt% H_2O) that is more consistent with about 5 wt% H_2O in the starting material, in line with the H_2O content determined by Raman spectroscopy. Following Ratajeski and Sisson (1999), which suggest that at high fO_2 (NNO + 1), loss of Fe to predominantly gold-based alloys is negligible (<2% relative) for a wide range of sample to capsule mass ratios. Wilke and Behrens (1999) concluded that BN jackets used as a buffer material for water-saturated experiments seems to be appropriate to avoid H_2O loss, but on the other hand, Sisson et al. (2005) and Kägi et al. (2005) demonstrated that the intrinsic fO_2 buffered by the 'sample-in-sample' double capsule technique is generally

Table 2 Experimental run conditions, phase assemblage and proportions

Run no.	Starting material	Initial H_2O wt%	T (°C)	P (GPa	Time (h)	Capsule technique	Assembly	Run products	Phase proportions wt%	H_2O (melt)	H_2O calc	ΣR^2	ΔFe%
RP30	8	8	1000	1.2	20	$Au_{90}Pd_{10}$-$Ag_{70}Pd_{30}$	NaCl-Pyrex-BN	liq	100 (21)	7.5	8.00	0.20	0.00
RP31	8	8	950	1.2	45	$Au_{90}Pd_{10}$-$Ag_{70}Pd_{30}$	NaCl-Pyrex-BN	liq, grt, amph, ilm	82.4 (17), 12.1 (76), 5.3 (42), 0.01 (5)	9.1	9.58	0.09	3.20
RP43	8	8	900	1.2	19	$Au_{90}Pd_{10}$-$Ag_{70}Pd_{30}$	NaCl-Pyrex-BN	liq, grt, amph, plg, ilm	61.3 (3), 11.3(8), 15.4 (13), 11.6 (3), 0.4 (1)	*8.7*	12.55	0.00	–3.70
RP39	8	8	850	1.2	63	$Au_{90}Pd_{10}$-$Ag_{70}Pd_{30}$	NaCl-Pyrex-BN	liq, grt, amph, plg	64.7 (21), 12.5 (13), 17.9 (73), 4.7 (59)	11.0	11.81	0.20	–0.54
RP37	6	6	1000	1.2	24	$Au_{90}Pd_{10}$-Pt[a]	NaCl-Pyrex-BN	liq, grt	93.1 (7), 6.9 (10)	5.4	6.35	0.06	15.60
RP90	6c	6	950	1.2	48	$Au_{90}Pd_{10}$	NaCl-Pyrex-BN	liq, grt, cpx, am	76.6 (21), 22.1 (35), 1.1 (21), trace	9.0	7.83	0.32	7.60
RP89	6c	6	900	1.2	42	$Au_{90}Pd_{10}$	NaCl-Pyrex-BN	liq, grt, amph	76.0 (24), 8.4 (54), 14.9 (64)	*11.0*	7.50	0.34	–6.67
RP62	4c	4	1000	1.2	49	$Au_{90}Pd_{10}$-Pt	NaCl-Pyrex-BN	liq, grt, cpx	90.8 (11), 8.0 (15), trace	5.2	4.65	0.36	1.52
RP26	4	4	950	1.2	49	$Au_{90}Pd_{10}$-$Ag_{70}Pd_{30}$	NaCl-Pyrex-BN	liq, grt, cpx	63.1 (32), 35.5 (49), 1.2 (33)	6.5	6.34	1.21	–0.12
RP62A	4c	4	900	1.2	48	$Au_{90}Pd_{10}$-Pt	NaCl-Pyrex-Al_2O_3-BN-MgO	liq, grt, cpx, plg, opx, ilm	41.9 (32), 13.2 (54), 4.9 (14), 31.9 (51), 7.2 (28), 0.8 (4)	*7.7*	9.88	0.09	–8.00
Rp88	4c	4	850	1.2	42	$Au_{90}Pd_{10}$	NaCl-Pyrex-BN	liq, grt, amph, plg, ilm	33.3 (26), 6.81 (44), 27.0 (55), 29.8 (26), <0.1	9.6	9.80	0.06	–6.51
RP66	8c	8	1000	0.8	48	$Au_{90}Pd_{10}$-Pt	NaCl-Pyrex-Al_2O_3-BN-MgO	liq	100 (4)	*5.5*	8.00	1.65	13.60
RP32	8	8	950	0.8	45	$Au_{90}Pd_{10}$-$Ag_{70}Pd_{30}$	NaCl-Pyrex-BN	liq, amph	92.9 (27), 7.1 (57)	7.6	8.46	0.76	–5.57
RP22	8	8	900	0.8	49	$Au_{90}Pd_{10}$-$Ag_{70}Pd_{30}$[a]	NaCl-Pyrex-BN	liq, grt, amph, plg, ilm	69.4 (28), 9.1 (18), 13.6 (24), 7.5 (10), 0.3 (9)	11.7	11.21	0.06	–0.10
RP25	8	8	850	0.8	20	$Au_{90}Pd_{10}$-$Ag_{70}Pd_{30}$[a]	NaCl-Pyrex-BN	liq, grt, amph, plg, ilm	66.9 (51), 3.8 (18),18.2 (10), 10.8 (8), 0.1 (1)	12.3	11.41	0.93	0.37
RP33	8	8	800	0.8	60	$Au_{90}Pd_{10}$-$Ag_{70}Pd_{30}$[a]	NaCl-Pyrex-BN	liq, grt, amph, plg, ilm	48.7 (4), 6.4 (14), 22.0 (7), 22.2 (6), 0.5 (1)	15.3	15.52	0.72	–1.40
RP18	6	6	950	0.8	48	$Au_{90}Pd_{10}$-$Ag_{70}Pd_{30}$	NaCl-Pyrex-BN	liq, grt, amph, plg, ilm	79.1 (23), 1.3 (46), 12.4 (38), 7.1, (21), 0.01 (6)	7.6	7.27	0.15	0.80
RP10	6	6	900	0.8	48	$Au_{90}Pd_{10}$-$Ag_{70}Pd_{30}$[a]	NaCl-Pyrex-BN	liq, grt, amph, plg, ilm	67.0 (31), 0.1 (29), 21.3 (59), 11.0, (21), 0.01 (6)	9.8	8.32	0.32	1.30
RP34	6	6	850	0.8	50	$Au_{90}Pd_{10}$-$Ag_{70}Pd_{30}$[a]	NaCl-Pyrex-BN	liq, amph, plg, ilm, grt[b]	58.5 (20), 26.7 (53), 14.4 (21), 0.4 (8)	10.6	9.55	0.37	0.77
RP13	6	6	800	0.8	63	$Au_{90}Pd_{10}$-$Ag_{70}Pd_{30}$[a]	NaCl-Pyrex-BN	liq, amph, plg, ilm	48.6 (56), 27.6 (10), 23.5 (50), 0.2 (17)	13.0	11.21	0.86	–3.64
RP36	6	6	800	0.8	60	$Au_{90}Pd_{10}$-$Ag_{70}Pd_{30}$[a]	NaCl-Pyrex-BN	liq, amph, plg, ilm	45.0 (33), 30.6 (68), 23.9 (25), 0.6 (13)	12.2	11.97	0.96	2.95
Rp67	4c	4	1000	0.8	48	$Au_{90}Pd_{10}$-Pt	NaCl-Pyrex-Al_2O_3-BN-MgO	liq, spl, mag	97.5 (4), 2.4 (5), < 0.1 (3)	4.0	4.10	0.31	5.58
RP14	4	4	950	0.8	49	$Au_{90}Pd_{10}$-$Ag_{70}Pd_{30}$[a]	NaCl-Pyrex-BN	liq, amph, plg, spl[c]	74.5 (16), 17.4 (16), 7.8 (11), trace	*7.6*	4.91	0.14	–0.71
RP15	4	4	900	0.8	49	$Au_{90}Pd_{10}$-$Ag_{70}Pd_{30}$[a]	NaCl-Pyrex-BN	liq, amph, plg, spl, ilm	68.3 (22), 21.7 (23), 8.9 (18), 0.9 (7), trace	*9.5*	5.29	0.26	0.03
RP40	4	4	850	0.8	46	$Au_{90}Pd_{10}$-$Ag_{70}Pd_{30}$	NaCl-Pyrex-BN	liq, amph, plg, ilm	53.6 (19), 25.0 (28), 20.6 (19), 0.9 (8)	*10.0*	6.53	0.68	–1.16

Values in Italics indicate >20% difference between theoretical and measured H_2O content as determined Raman spectroscopy

ΔFe% apparent gain or loss of iron, calculated as: 100 × (total Fe_{calc} − total FeO in the starting material)/total FeO in the starting material. Positive values: iron gain, negative values, iron loss; *H_2O (melt)* H_2O content determined by Raman spectroscopy, applying the measurement protocol of Di Muro et al. (2006), and Mercier et al. (2008); *H_2O calc* theroretical H_2O content of the silicate liquid determined by the starting material and the appropriate proportions of H_2O incorporated into hydrous minerals

[a] Fe-presaturated inner Au-Pd capsule, following techniques described by Kägi et al. (2005)

[b] Garnet is present but was not used for mass balance (negative)

[c] Spinel is present, but too small for analysis, spinel from RP15 was therefore used for the mass balance

overcome by the buffering capacity of BN. In order to avoid H_2O loss, we used the piston-cylinder assemblies similar to those of Kägi et al. (2005); Fig. 2b, BN setup). Experimental conditions ranged between 800 and 1,000°C and 0.8–1.2 GPa and run durations varied from 24 to 60 h (Table 2). Most experiments conducted in this study employing the double capsule technique have been performed with a combination of $Au_{90}Pd_{10}$ (inner) and Pt or $Ag_{70}Pd_{30}$ (outer) capsules. Duplicate experiments at identical pressure−temperature−X_{H_2O} conditions (e.g. rp13 and rp36; see Table 2), in general, resulted in very similar melt fractions, phase assemblages and phase compositions indicating good reproducibility of the results. Previous experimental studies on tonalite or andesite bulk compositions with H_2O and H_2O–CO_2 mixtures were often performed in $Ag_{70}Pd_{30}$ capsules in the range of 1–3 GPa (Allen and Boettcher 1978, 1983; Allen et al. 1975; Green 1972; Green and Ringwood 1968a; Huang and Wyllie 1986; Stern et al. 1975). Due to the choice of single capsule non-pretreated alloys as capsule material, the results of these earlier studies, however, must be carefully evaluated for H_2O loss and/or oxidation problems, before they can directly be compared with our new experiments.

Recovered capsules were mounted in epoxy resin, ground with sandpaper to expose a longitudinal cross-section of the charge, and polished with diamond paste of different grades. After carbon coating, major element compositions of experimental liquids and solid phases were determined with a Cameca SX50 and a JEOL 8600 electron microprobe analyzer at ETH Zürich. We employed an accelerating voltage of 15 kV and a beam current of 20 nA, using silicates and oxides as standards. Analytical errors associated with Na loss in hydrous SiO_2-rich glasses during microprobe analysis have been minimized by reducing the probe current to 7 nA, increasing the spot size to 10 μm and limiting the counting time to 3 s for Na. Results on experimental glasses and minerals are listed in Table 3.

Bulk H_2O and CO_2 contents of some of the starting materials were determined by Fourier transform infrared spectroscopy (FT-IR) at Caltech on rapidly fused starting material at high pressures (Table 4). Powders were packed into single $Au_{90}Pd_{10}$ capsules, redried overnight at 110°C and then sealed by arc welding. Samples were hold at 1.6 GPa and 1,150°C, for 30 min, yielding crystal and bubble-free glasses. Absorption spectra were measured on glass wafers prepared from the center of the capsules. Concentrations were determined through the Beer-Lambert law with absorbance from composition-dependent expressions for the 1,430 cm^{-1} absorption band for CO_3^{2-}, and for the 3,500 and 5,200 cm^{-1} for H_2O. Resulting bulk

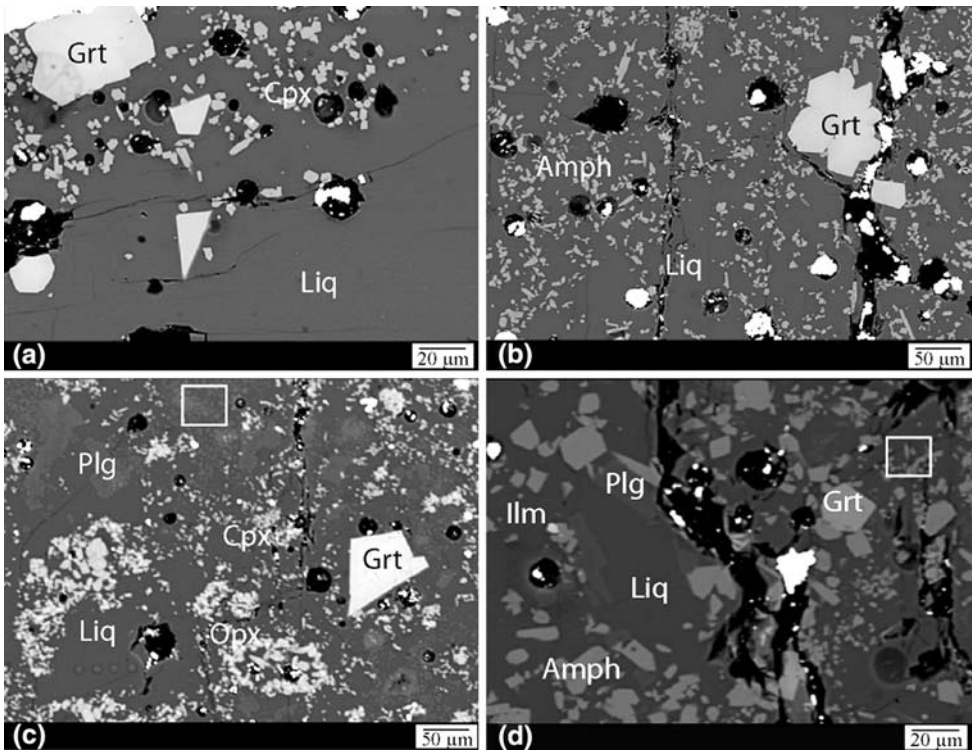

Fig. 2 Backscatter electron images (BSE) of run products. Phases identified in the experiments include garnet (Grt), high-Ca pyroxene (Cpx), low-Ca pyroxene (Opx), amphibole (Amph), plagioclase (Plg), ilmenite (Ilm) and melt (Liq). **a** Run RP90 (garnet + cpx + liquid), 1.2 GPa, 6 wt% H_2O and 950°C; **b** Run RP89, (garnet + amphibole + liquid), 1.2 GPa, 6 wt% H_2O and 900°C; **c** Run RP62A (garnet + clinopyroxene + orthopyroxene + plagioclase + liquid) at 1.2 GPa, 6 wt% H_2O and 950°C; **d** Run RP18 (garnet + amphibole + plagioclase + liquid) at 0.8 GPa, 6 wt% H_2O and 950°C; The *boxes* highlight needle-like crystal and subhedral quench plagioclases. The majority of the experiments contain traces of ilmenite and/or spinel. *Scale bar* is 20–50 µm. Note the overall small grain size (except for garnet). Note also that abundant bubbles (~5 to >10 µm) can be observed, indicating vapor saturation of most of the experiments

water and CO_2 contents were determined following the procedures of Dixon et al. (1995) for H_2O and Pilet et al. (2008) for CO_2 and are listed in Table 4. Resulting CO_2 contents (~0.9 wt%) are higher than expected for our starting material, but consistent with the observation that many experimental runs contain small bubbles indicating saturation with a fluid phase. However, the CO_2 concentrations are likely to be lower for the andesite experiments at 0.8 and 1.2 GPa, because the experiments on the starting material were run after the phase equilibrium experiments were terminated. Since we used synthetic starting materials, there are several potential sources of CO_2, such as incomplete degassing of $CaCO_3$ during preparation of the starting material, traces of hydrocarbon left from the denatured ethanol during grinding (see also Sisson et al. 2005), or decarbonated CaO progressively recarbonates by fixing CO_2 from the air.

The H_2O contents of all experiments were determined by Micro-Raman spectroscopy. Raman scattering was excited using a 488 nm Ar + Laser (Inova 90) and measurements were performed with a LabRam II Micro-Raman spectrometer at ETH Zurich. Glasses were analyzed by focusing the laser beam on the sample surface, with ~1–2 mm spotsize under an Olympus microscope in confocal mode. The instrument is equipped with a beam splitter that allows 70% of the scattered light to reach the detector after passing through a notch filter. Spectra were obtained in the 200–1,500 and 2,800–3,900 cm^{-1} ranges to cover low and high frequency T-O stretching and vibration modes and the OH/H_2O stretching regions. Average input laser power was about 600 mW. Spectra acquisition times were 120 s; three measurements were conducted on each spot and three different spots were analyzed on each sample. We did not apply Long-correction to our raw data as this does not improve the water calibration (see Mercier et al. 2008) and performed a cubic baseline correction scheme along the strategies described by Di Muro et al. (2006) and Mercier et al. (2008). Calibration was conducted with a series of internal standard glasses ranging from basalts to andesites to rhyolites and H_2O contents from 0.0 to 11.0 wt% that have been measured by FTIR, SIMS and/or Karl–Fisher titration (KFT). The calibration bases on the evaluation of

Table 3 Electron microprope analyses of run products, with all Fe as FeO

Run no.	Phase	*n*	SiO_2	TiO_2	Al_2O3	FeO_{tot}	MnO	MgO	CaO	Na_2O	K_2O	Total	Mg#
RP30	gl	11	53.0 (8)	0.69 (5)	15.5 (5)	6.2 (4)	0.26 (8)	2.35 (12)	6.68 (28)	2.33 (17)	1.23 (9)	88.3	0.403
RP31	gl	18	55.3 (8)	0.68 (7)	15.4 (2)	5.91 (18)	0.22 (5)	1.60 (8)	6.04 (17)	2.88 (16)	1.45 (8)	89.5	0.325
	grt	15	38.3 (4)	1.07 (9)	20.1 (2)	21.6 (12)	2.14 (7)	8.02 (26)	9.08 (33)	0.04 (2)	0.01 (1)	100.4	0.398
	amph	16	41.0 (7)	1.51 (25)	15.1 (6)	13.8 (9)	0.36 (3)	11.6 (8)	10.8 (3)	2.13 (8)	0.78 (3)	97.0	0.601
	ilm	6	0.03 (1)	40.4 (18)	0.69 (6)	53.0 (26)	0.52 (8)	2.33 (19)	0.08 (1)	0.01 (1)	0.01 (0)	96.7	0.068
RP43	gl	12	61.6 (6)	0.50 (7)	16.4 (3)	3.26 (18)	0.06 (5)	0.82 (6)	4.87 (12)	3.08 (22)	1.90 (8)	92.5	0.309
	grt	8	38.3 (2)	1.12 (10)	20.3 (2)	23.3 (6)	1.54 (21)	6.81 (29)	9.13 (45)	0.02 (1)	0.01 (1)	100.5	0.343
	amph	16	40.7 (7)	1.65 (33)	15.0 (4)	16.5 (6)	0.25 (4)	10.1 (6)	10.5 (3)	2.08 (7)	0.70 (7)	97.4	0.521
	plg	4	52.3 (2)	0.08 (4)	29.4 (1)	0.35 (36)	0.01 (1)	0.07 (4)	12.7 (4)	4.02 (18)	0.24 (0)	100.3	0.082
	ilm	5	0.11 (10)	43.7 (17)	0.73 (8)	50.4 (14)	0.21 (3)	2.32 (13)	0.18 (8)	0.01 (1)	0.02 (1)	97.7	0.076
RP39	gl	10	60.3 (7)	0.30 (6)	16.5 (4)	2.31 (23)	0.06 (5)	0.54 (6)	5.02 (20)	2.88 (19)	1.67 (6)	89.5	0.294
	grt	11	37.9 (6)	1.24 (14)	20.1 (3)	23.2 (15)	1.55 (26)	4.39 (35)	11.7 (4)	0.05 (2)	0.02 (2)	100.1	0.252
	amph	7	40.5 (9)	1.31 (11)	15.2 (6)	16.8 (6)	0.35 (71)	9.4 (6)	10.9 (3)	2.22 (8)	0.82 (5)	97.4	0.500
	plg	7	49.4 (7)	0.06 (5)	31.8 (8)	0.74 (29)	0.02 (1)	0.08 (5)	15.1 (7)	2.33 (25)	0.19 (6)	99.8	0.159
RP37	gl	26	53.0 (7)	0.83 (6)	16.8 (3)	7.8 (4)	0.26 (6)	2.38 (11)	6.57 (18)	2.95 (16)	1.43 (6)	92.1	0.352
	grt	21	39.5 (5)	0.79 (39)	21.5 (3)	19.5 (8)	1.60 (21)	9.45 (66)	7.72 (80)	0.02 (2)	0.02 (2)	100.4	0.464
RP90	gl	23	56.7 (3)	0.75 (4)	16.5 (2)	4.01 (10)	0.11 (3)	1.20 (5)	5.52 (13)	2.62 (6)	1.60 (4)	89.0	0.349
	grt	14	38.6 (3)	1.46 (14)	20.2 (2)	20.7 (4)	1.44 (25)	7.28 (39)	9.70 (37)	0.03 (2)	0.01 (1)	99.4	0.385
	cpx	7	46.9 (3)	1.07 (5)	9.14 (24)	10.7 (4)	0.30 (8)	10.0 (1)	20.3 (3)	0.59 (3)	0.02 (1)	99.0	0.627
RP89	gl	18	54.8 (4)	0.57 (4)	16.4 (2)	3.23 (11)	0.14 (3)	0.77 (4)	5.55 (10)	2.20 (38)	1.43 (5)	85.1	0.298
	grt	19	37.5 (4)	1.45 (7)	20.4 (2)	21.5 (4)	2.04 (26)	5.55 (20)	10.2 (4)	0.05 (2)	0.01 (1)	98.7	0.315
	amph	7	40.0 (6)	1.85 (10)	16.0 (8)	15.5 (5)	0.37 (3)	9.48 (47)	10.6 (2)	1.90 (6)	0.82 (4)	96.5	0.522
RP62	gl	10	55.4 (3)	0.87 (2)	16.6 (1)	6.91 (14)	0.17 (2)	1.93 (6)	6.67 (6)	2.58 (7)	1.52 (3)	92.6	0.332
	grt	5	39.0 (4)	1.12 (25)	20.7 (3)	19.9 (1)	1.36 (14)	9.33 (24)	7.98 (38)	0.03 (3)	<0.01	99.4	0.455
	cpx	7	48.3 (8)	0.71 (9)	7.8 (7)	11.2 (8)	0.40 (6)	12.2 (6)	19.2 (3)	0.60 (2)	0.04 (2)	99.0	0.639
RP26	gl	13	61.0 (3)	0.75 (3)	15.6 (1)	4.29 (6)	0.09 (2)	1.03 (3)	5.07 (5)	2.90 (22)	1.85 (2)	92.5	0.300
	grt	5	38.5 (3)	1.50 (21)	20.2 (3)	23.5 (8)	1.55 (11)	7.4 (8)	8.05 (34)	0.04 (2)	<0.01	100.7	0.359
	cpx	4	48.1 (8)	0.85 (3)	8.32 (60)	12.3 (6)	0.29 (9)	10.5 (3)	18.5 (7)	0.71 (8)	<0.01	99.6	0.604
RP62A	gl	25	62.8 (11)	0.45 (5)	14.7 (7)	2.84 (56)	0.05 (4)	0.90 (57)	4.12 (92)	2.46 (25)	2.32 (13)	90.6	0.362
	grt	28	38.3 (8)	1.50 (20)	20.3 (9)	24.5 (11)	1.46 (46)	6.11 (86)	8.40 (50)	0.05 (3)	<0.01	100.7	0.308
	cpx	12	48.8 (10)	0.64 (10)	6.53 (56)	16.2 (15)	0.50 (10)	10.1 (8)	16.4 (16)	0.64 (11)	0.07 (5)	100.0	0.526
	plg	19	55.5 (10)	0.04 (3)	27.1 (9)	0.52 (38)	<0.02	<0.04	10.6 (8)	4.74 (31)	0.36 (7)	98.9	0.175
	opx	6	48.6 (8)	0.31 (3)	5.90 (98)	26.4 (8)	0.72 (10)	15.7 (9)	1.79 (27)	0.07 (4)	0.05 (3)	99.6	0.513
	ilm	9	0.44 (11)	48.6 (10)	0.51 (4)	43.0 (2)	0.31 (0)	3.6 (2)	0.29 (1)	0.01 (1)	0.05 (0)	96.9	0.131
RP88	gl	18	65.8 (7)	0.23 (3)	13.7 (2)	1.94 (11)	0.09 (4)	0.26 (4)	3.30 (10)	1.01 (46)	1.98 (12)	88.3	0.196
	grt	17	37.6 (8)	1.32 (18)	19.2 (10)	22.9 (6)	3.21 (51)	3.76 (40)	10.5 (7)	0.07 (6)	<0.01	98.5	0.226
	amph	19	41.4 (5)	1.67 (17)	13.6 (6)	18.1 (7)	0.49 (6)	8.48 (38)	10.4 (3)	1.73 (7)	0.69 (5)	96.6	0.455
	plg	9	55.6 (10)	0.03 (2)	26.4 (7)	0.39 (10)	0.02 (2)	<0.03	9.66 (89)	5.21 (36)	0.31 (5)	97.7	0.000
RP66	gl	15	52.6 (2)	0.86 (5)	17.2 (2)	8.23 (16)	0.38 (4)	2.78 (7)	7.25 (9)	2.55 (9)	1.32 (5)	93.2	0.376
RP32	gl	11	54.0 (4)	0.84 (8)	16.1 (2)	6.20 (36)	0.26 (9)	2.03 (12)	6.26 (16)	2.92 (12)	1.47 (5)	90.2	0.368
	amph	7	42.5 (4)	2.92 (4)	12.5 (2)	12.5 (3)	0.40 (2)	13.2 (2)	10.5 (2)	2.24 (3)	0.51 (4)	97.1	0.653
RP22	gl	5	59.4 (1)	0.46 (7)	16.3 (3)	3.62 (11)	0.16 (4)	1.00 (9)	5.37 (21)	2.30 (10)	1.62 (18)	90.3	0.331
	grt	5	39.0 (2)	0.87 (1)	21.1 (2)	24.4 (8)	2.62 (27)	5.88 (29)	7.53 (51)	0.03 (2)	<0.01	101.4	0.300
	amph	3	42.1 (3)	1.91 (21)	13.9 (5)	17.3 (4)	0.39 (5)	10.4 (3)	10.1 (1)	1.84 (1)	0.58 (4)	98.6	0.521
	pl	22	47.4 (6)	0.05 (3)	33.9 (6)	0.40 (13)	0.03 (2)	0.09 (1)	17.3 (8)	1.39 (29)	0.12 (5)	100.9	0.203
	ilm	5	0.13 (7)	51.9 (3)	0.24 (1)	42.2 (5)	1.35 (32)	3.08 (2)	0.20 (4)	<0.02	<0.01	99.0	0.116

Table 3 continued

Run no.	Phase	*n*	SiO_2	TiO_2	Al_2O3	FeO_{tot}	MnO	MgO	CaO	Na_2O	K_2O	Total	Mg#
RP25	gl	7	59.7 (6)	0.40 (15)	16.0 (4)	4.37 (326)	0.22 (5)	0.75 (10)	5.23 (22)	2.36 (16)	1.84 (24)	90.9	0.233
	grt	3	37.6 (2)	0.79 (1)	20.2 (1)	25.5 (1)	2.56 (17)	4.15 (05)	8.91 (7)	0.02 (01)	<0.01	99.8	0.225
	amph	9	42.1 (9)	1.56 (27)	14.1 (10)	18.3 (7)	0.42 (5)	8.97 (61)	10.3 (5)	1.85 (13)	0.63 (3)	98.3	0.466
	pl	4	48.2 (6)	0.03 (1)	32.4 (6)	0.56 (11)	0.04 (1)	0.03 (2)	16.8 (3)	1.93 (12)	0.13 (5)	100.2	0.094
	ilm	5	0.21 (12)	50.9 (6)	0.26 (4)	44.0 (6)	1.23 (5)	1.95 (1)	0.17 (5)	<0.01	<0.01	98.7	0.073
RP33	gl	6	67.6 (9)	0.14 (2)	13.6 (3)	2.18 (218)	0.10 (5)	0.37 (6)	2.66 (216)	2.64 (20)	2.37 (10)	91.7	0.232
	grt	8	37.4 (2)	1.03 (8)	19.6 (2)	27.9 (13)	2.86 (22)	3.60 (24)	8.16 (71)	0.04 (02)	0.02 (1)	100.6	0.187
	amph	9	43.1 (9)	1.12 (21)	12.8 (8)	18.5 (14)	0.45 (5)	8.76 (78)	10.3 (4)	1.61 (8)	0.63 (6)	97.2	0.458
	pl	6	47.5 (10)	0.04 (2)	33.5 (7)	1.15 (31)	0.04 (3)	0.07 (2)	15.7 (5)	1.73 (20)	0.18 (6)	99.9	0.094
	ilm	3	0.55 (27)	48.7 (2)	0.23 (2)	46.0 (2)	0.79 (1)	1.13 (5)	0.16 (3)	0.05 (2)	0.04 (2)	97.6	0.042
RP18	gl	26	55.7 (7)	0.68 (4)	16.6 (2)	6.00 (46)	0.30 (2)	1.57 (13)	5.80 (18)	2.55 (9)	1.51 (7)	90.7	0.318
	grt	5	37.6 (8)	1.32 (18)	19.2 (10)	22.9 (6)	3.21 (51)	3.76 (40)	10.5 (7)	0.07 (6)	<0.01	98.5	0.226
	amph	5	41.4 (5)	1.97 (35)	14.1 (3)	16.9 (14)	0.41 (5)	10.1 (9)	10.0 (3)	2.09 (9)	0.57 (4)	97.4	0.515
	pl	6	48.3 (10)	0.05 (0)	31.9 (5)	0.82 (23)	0.04 (1)	0.18 (6)	16.1 (7)	1.93 (30)	0.16 (2)	99.5	0.284
	ilm	2	0.40 (24)	50.5 (2)	0.34 (2)	42.6 (2)	1.13 (1)	3.32 (3)	0.45 (6)	<0.02	<0.01	98.8	0.122
RP10	gl	7	57.9 (6)	0.43 (2)	15.9 (1)	4.91 (7)	0.21 (2)	0.79 (4)	4.71 (11)	2.46 (12)	1.80 (3)	89.1	0.223
	grt	7	37.4 (4)	0.90 (10)	20.3 (3)	24.9 (11)	2.78 (10)	4.86 (16)	8.45 (26)	0.03 (1)	<0.01	99.6	0.258
	amph	15	41.5 (4)	2.24 (19)	13.1 (4)	19.1 (8)	0.53 (8)	9.14 (16)	9.82 (23)	2.12 (6)	0.60 (5)	98.1	0.460
	pl	8	44.6 (5)	0.02 (2)	34.9 (7)	0.75 (54)	0.04 (2)	0.06 (4)	17.8 (4)	1.32 (17)	0.07 (1)	99.6	0.129
	ilm	3	0.13 (10)	51.1 (4)	0.27 (4)	44.0 (3)	1.03 (3)	2.01 (2)	0.13 (5)	0.07 (5)	<0.01	98.3	0.075
RP34	gl	11	62.6 (5)	0.26 (4)	16.3 (3)	3.62 (17)	0.15 (6)	0.51 (8)	4.20 (33)	2.72 (27)	2.63 (28)	92.9	0.189
	grt	6	37.9 (3)	0.95 (5)	20.3 (2)	25.1 (5)	3.10 (20)	3.79 (16)	8.77 (44)	0.02 (1)	<0.01	99.9	0.212
	amph	9	40.7 (4)	1.46 (25)	14.2 (4)	19.9 (5)	0.48 (4)	7.70(24)	9.94 (35)	2.12 (11)	0.61 (4)	97.1	0.377
	pl	6	48.4 (8)	0.03 (1)	32.6 (9)	0.71 (62)	0.03 (2)	0.04 (2)	15.6 (7)	2.17 (28)	0.13 (3)	99.7	0.084
	ilm	4	0.13 (5)	50.1 (2)	0.25 (3)	44.9 (4)	0.96 (1)	1.46 (4)	0.21 (9)	0.03 (1)	<0.01	98.0	0.054
RP13	gl	10	63.4 (1)	0.12 (2)	13.8 (7)	1.86 (8)	0.13 (1)	0.27 (4)	2.50 (5)	2.16 (3)	2.43 (1)	86.6	0.205
	amph	14	43.1 (7)	1.22 (32)	11.8 (7)	22.3 (13)	0.54 (3)	6.84 (69)	9.9 (3)	1.65 (8)	0.61 (7)	97.9	0.353
	pl	7	47.9 (13)	0.02 (2)	33.8 (12)	0.65 (40)	0.03 (2)	0.07 (2)	15.9 (6)	2.25 (31)	0.10 (2)	100.7	0.156
	ilm	3	0.40 (14)	51.7 (10)	0.19 (6)	44.4 (4)	1.28 (1)	1.02 (3)	0.13 (3)	0.04 (3)	<0.01	99.2	0.039
RP36	gl	12	69.7 (6)	0.12 (1)	13.1 (1)	1.75 (1)	0.12 (8)	0.17 (11)	1.88 (1)	1.94 (50)	3.62 (1)	92.4	0.148
	amph	9	43.5 (7)	1.42 (8)	13.1 (2)	19.5 (5)	0.66 (10)	8.27 (66)	9.66 (39)	1.84 (5)	0.59 (7)	98.4	0.431
	pl	2	44.3 (2)	0.07 (1)	35.0 (1)	3.25 (16)	0.11 (1)	0.24 (1)	15.9 (2)	1.61 (5)	0.08 (1)	100.5	0.116
	ilm	2	1.21 (39)	53.5 (38)	0.28 (8)	41.3 (20)	1.28 (1)	1.24 (10)	0.06 (2)	0.10 (1)	0.07 (1)	99.0	0.051
RP67	gl	15	53.5 (13)	0.79 (21)	16.4 (3)	7.19 (13)	0.33 (5)	2.86 (9)	7.08 (11)	2.46 (11)	1.45 (6)	92.1	0.414
	spl	2	0.04 (1)	0.29 (1)	51.0 (1)	33.9 (3)	0.56 (4)	13.17 (2)	0.17 (2)	<0.01	<0.01	99.1	0.410
	mag	13	0.15 (4)	4.52 (6)	8.02 (9)	77.4 (4)	0.60 (2)	3.68 (5)	0.14 (9)	<0.01	<0.01	94.6	0.078
RP14	gl	6	54.7 (4)	0.57 (3)	16.41 (1)	5.88 (4)	0.25 (4)	1.25 (3)	5.08 (9)	2.46 (11)	1.82 (3)	88.4	0.274
	amph	19	42.3 (8)	2.42 (29)	14.3 (4)	14.7 (5)	0.37 (4)	10.9 (5)	10.4 (3)	2.19 (9)	0.48 (12)	98.0	0.569
	pl	6	48.8 (5)	0.08 (2)	31.7 (7)	1.13 (20)	0.05 (1)	0.22 (4)	15.8 (4)	1.95 (9)	0.13 (9)	99.8	0.256
RP15	gl	17	58.6 (8)	0.40 (6)	16.3 (9)	4.45 (32)	0.20 (4)	0.90 (15)	4.64 (70)	2.44 (23)	1.81 (14)	89.7	0.264
	amph	7	41.9 (3)	1.61 (32)	13.1 (3)	17.5 (11)	0.41 (5)	9.9 (5)	10.3 (4)	1.86 (4)	0.65 (3)	97.1	0.502
	plg	12	46.2 (9)	0.02 (1)	33.6 (5)	0.71 (24)	0.03 (2)	0.09 (7)	16.9 (5)	1.61 (30)	0.10 (5)	99.2	0.189
	ilm	5	0.22 (15)	50.9 (2)	0.31 (1)	43.9 (5)	1.03 (2)	2.27 (4)	0.08 (2)	0.04 (3)	<0.01	98.7	0.084
	spl	5	0.12 (8)	0.16 (0)	58.1 (18)	35.6 (7)	0.54 (1)	4.94 (53)	0.19 (9)	<0.01	<0.01	99.6	0.198

Table 3 continued

Run no.	Phase	*n*	SiO_2	TiO_2	Al_2O3	FeO_{tot}	MnO	MgO	CaO	Na_2O	K_2O	Total	Mg#
RP40	gl	17	62.5 (9)	0.23 (5)	14.7 (3)	3.35 (36)	0.16 (6)	0.42 (8)	3.56 (25)	2.84 (25)	2.12 (5)	89.9	0.182
	amph	10	41.9 (7)	1.40 (21)	12.4 (8)	19.5 (14)	0.49 (15)	7.3 (9)	10.4 (4)	1.92 (17)	0.58 (9)	96.4	0.414
	plg	8	48.7 (10)	0.05 (2)	32.6 (9)	1.12 (34)	0.04 (2)	0.06 (4)	15.7 (6)	1.81 (18)	0.17 (5)	100.3	0.087
	ilm	8	0.11 (9)	47.8 (11)	0.33 (4)	49.3 (8)	0.98 (8)	1.24 (2)	0.10 (2)	<0.02	<0.01	99.8	0.043

Units in parentheses indicate standard deviation from average analyses, in terms of significant digits and should be read as, e.g. 53.0 ± 0.8 wt%

Table 4 FT-IR results on starting materials synthesized at 1.6 GPa, 1150°C for 30 minutes

Starting material	Run No.	H_2O initial	*r* (g/cm-3)	*t* H_2O^a	Mol. abs.[d]	H_2O^a	*t* H_2O^b	Mol. abs.[d]	H_2O^b	H_2O^c	*t* CO_2	Mol. abs.[e]	CO_2
F8a-8c	PU 979	8.14	2.65	145	0.62	6.3 (35)	24	63	6.17 (13)	~6.2	24	305	0.89 (2)
F8a-6c	PU 980	6.14	2.65	103	0.62	9.6 (3)	33	63	9.4 (6)		33	305	0.88 (3)
F8a-4c	PU 981	4.14	2.65	46	0.62	7.7 (3)	28	63	7.3 (3)	~6.8	28	305	0.93 (3)

All FT-IR results correspond to an average of four measurements at distinct locations

t thickness of the glass wafer (in mm) used for H_2O total, H_2O molecular and CO_2 measurements, respectively; *r* calculated density of hydrous silicate glasses

[a] H_2O is calculated from the molecular H_2O band at 5,200 cm^{-1}

[b] H_2O is calculated from the total H_2O band at 3,530 cm^{-1}

[c] H_2O determined by Raman spectroscopy

[d] The molar absorptivity of H_2O molecular bands at 5,200 cm^{-1}, and total H_2O at 3,530 cm^{-1} was determinated by Dixon et al. (1995) and Newmann et al. (2000), respectively

[e] The molar absorptivity of the carbonate bands at 1,430 cm^{-1} (305 l/mol cm) was calculated for an andesitic composition using the parameterization of Dixon and Pan (1995)

the peak heights for the OH/H_2O band intensity (around 3,500 cm^{-1}) compared to the intensity ratio of the low frequency (LF, 400–600 cm^{-1}) over the high frequency (HF, 800–1,200 cm^{-1}) T-O bands corrected with an algorithm taking into account the composition (polymerization) dependence of the LF/HF ratio as a function of NBO/T (non-bridging oxygens per tetrahedrally coordinated cation, Mysen 1988). Estimated accuracy of the H_2O-determination using the described analytical procedure based on standard reproducibility and variability is in the order 0.5–1.0 wt% H_2O. Results of quantitative H_2O determinations of all experimental runs are listed in Table 2, and a comparison of H_2O determinations by FT-IR and Raman spectroscopy are shown in Table 4. The good agreement between FT-IR and Raman spectroscopic measurements suggests that the H_2O contents of experimental runs as determined by Raman spectroscopy are probably accurate to ±20%.

Experimental results

H_2O-undersaturated experiments were conducted at 0.8 and 1.2 GPa in a temperature range of 800–1,000°C, and H_2O contents of 4, 6 and 8 wt%. For simplicity, we will refer to low-pressure experiments for those performed at 0.8 GPa, and to high-pressure experiments for those at 1.2 GPa. From the 25 equilibrium crystallization experiments reported in this study, nine have been performed with initial H_2O contents of 8 wt%, eight with 6 wt% H_2O, and eight with 4 wt% H_2O. Phases identified in the experiments include garnet (grt), clinopyroxene (cpx), orthopyroxene (opx), amphibole (amph), plagioclase (plg), ilmenite (ilm), spinel (spl) and liquid (liq). Generally, quench-free glasses (50–100 μm pools) were obtained for experiments at temperatures exceeding 900°C, while at lower temperatures, the degree of crystallization increases and quench-free areas are usually smaller than 50 μm. Average liquid and solid phase major element compositions with their standard deviations are reported in Table 3. Quantitative measurements and BSE images reveal homogeneous glasses (Fig. 2). Inspection of BSE images showed that many of the experimental glasses contain relatively large and abundant vesicles of tens of micrometer in diameter, indicating that the majority of the experimental runs were vapor-saturated with a CO_2–H_2O fluid, consistent with the relatively high initial CO_2 contents. These observations are summarized in Table 2.

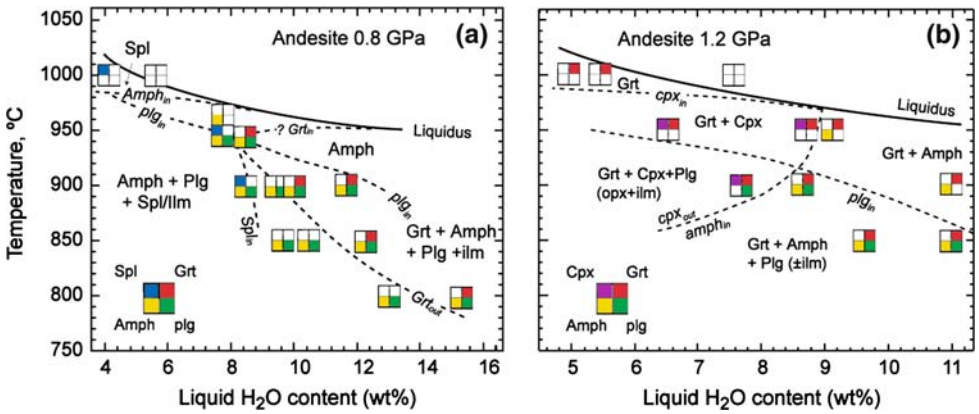

Fig. 3 Isobaric T-X(H_2O) phase diagrams for andesitic liquids **a** 0.8 GPa, and **b** 1.2 GPa. *Dashed lines* show the phase in/out boundaries derived from this study. Note that garnet-in at 0.8 GPa is assumed. garnet *Grt,* clinopyroxene *Cpx,* orthopyroxene *Opx,* amphibole *Amph,* plagioclase *Plg,* ilmenite Ilm, spinel *Spl*, liquid *Liq*

Homogeneous and euhedral to subhedral crystals exhibit no significant major element zoning as illustrated by the small relative errors on the major element composition (Table 3). The grain size of garnet can reach up to 100 μm in diameter; amphibole and plagioclase are usually between 10 and 30 μm in size, whereas pyroxenes and oxides tend to be smaller than 10 μm. Phase proportions are calculated by mass balance using respective bulk compositions (Table 1) and experimental phase compositions (Table 3) and a least squares regression routine implemented in the EXCEL® program. The principal phase relations at 0.8 and 1.2 GPa are illustrated in $T - X_{H_2O}$ diagrams in Fig. 3.

Phase relations at 0.8 GPa

At low-pressure (Fig. 3a), the liquidus temperature of the andesite is located below 1,000°C at 8 wt% H_2O and above 1,000°C at 6 and 4 wt%. H_2O. At 8 wt% H_2O, the melt fraction (*f*) decreases from 1 to 0.49 with decreasing temperature from 1,000 to 800°C. Amphibole is the (first) liquidus phase and appears between 1,000° and 950°C followed by garnet, plagioclase and ilmenite at 900°C. The assemblage composed of garnet, amphibole, plagioclase and ilmenite remains stable down to temperatures of 800°C (Table 2 for details on phase proportions). With decreasing melt fraction, the amphibole/plagioclase ratio decreases slightly. This is observed in all series at 0.8 GPa. At 6 wt% H_2O, *f* decreases from 0.8 to 0.45 with decreasing temperature (950–800°C); garnet, amphibole, plagioclase and ilmenite constitute the liquidus phases at 950°C down to temperatures of 850°C. At 800°C, garnet disappeared, and amphibole, plagioclase and ilmenite form the phase assemblage. At 4 wt% H_2O, *f* decreases from 0.97 to 0.53 with decreasing temperature (1,000–850°C). In this series, garnet is not present at any temperature examined. As noted by Helz (1982), the thermal stability of amphibole increases and the field of amphibole plus liquid expands (in basaltic systems) with increasing H_2O contents, consistent with our results.

Phase relations at 1.2 GPa

At high-pressure (Fig 3b) and 8 wt% H_2O, the melt fraction decreases systematically from 1 to 0.65 with decreasing temperature from 1,000 to 850°C. The liquidus at these conditions is located around 1,000°C, ($f = 1$) with garnet and amphibole as the first liquidus phases observed at 950°C, followed by plagioclase at 850°C. Traces of ilmenite can be found (<0.01 wt%). At 6 wt% H_2O, *f* decreases from 0.93 to 0.76 with decreasing temperature (1,000–900°C); the liquidus temperature is above 1,000°C. The first liquidus phase is garnet at 1,000°C, followed by clinopyroxene and traces of amphibole at 950°C. Amphibole is abundant at 900°C (14.9 wt%), suggesting that the cpx-amphibole reaction boundary is close to 950°C, (Fig. 3b). The stability field of clinopyroxene at 6 wt% H_2O is limited to the 900°C experiment. At high-pressure and 4 wt% H_2O, *f* decreases from 0.91 to 0.33 with decreasing temperature (1,000–850°C); the liquidus temperature is above 1,000°C. Garnet and cpx are the first liquidus phase at 1,000°C followed by cpx at 950°C and by plagioclase together with two pyroxenes and trace amounts of ilmenite (0.8 wt%) at 900°C. At 850°C, garnet, amphibole and plagioclase are the crystallizing phases. We conclude that at high-pressure (1.2 GPa) garnet is an important phase over the entire range of conditions (800–1,000°C, 4–8 wt% H_2O). The stability field of amphibole is dependent on the H_2O content in the melt: it is stable at high H_2O contents to high temperatures and extends to low temperature–low H_2O contents (850°C, 4 wt% H_2O). On the contrary, increasing H_2O contents shift plagioclase crystallization to lower temperatures, as observed in many other experimental studies (e.g. Sisson and Grove 1993a). The stability field of clinopyroxene is small compared to the other phases and is restricted to high temperatures exceeding 900°C and to medium to low H_2O-contents (4–6 wt%). Orthopyroxene appears only at 900°C and 4 wt% H_2O. Ilmenite and spinel are present all over the studied range as minor phases (<0.4 wt%). For the following

section on mineral compositions and related discussions, we have exclusively utilized those runs that suffered none or only minimal H_2O loss (e.g. rp15 and rp13). Since the H_2O content is one of the main variables that control the phase relations, we have reported experiments, which have suffered minor water loss, rp43 and rp88, with the perspective that an experiment with 8 wt% initial H_2O that suffered minor H_2O-loss mimics an experiment with ~5 wt% initial H_2O (rp 43).

Mineral compositions

Garnet

Endmember compositions of the experimental garnets are illustrated in Fig. 4 and compared to data from basaltic systems (Alonso-Perez 2006; Müntener et al. 2001) and natural occurrences from island arcs. For a given pyrope content, low-pressure garnets are generally richer in almandine + spessartine and lower in grossular component than high-pressure ones. The effect of H_2O on garnet compositions is not dramatic, but results in a tendency of increasing grossular content with increasing amounts of dissolved H_2O in the liquid. Garnet compositions of our study resemble those of "group C" (Coleman et al. 1965, garnets present in granulites) and are similar to granulite garnets commonly found, but not restricted to, subduction environments, such as those in Northern Fiordland, New Zealand (Schröter et al. 2004), deep-crustal xenoliths form the Northern Andes (Weber et al. 2002) or garnet cumulates from the Jijal complex, Kohistan arc (Ringuette et al. 1999, Müntener et al. unpublished data). Variations of garnet Mg# expressed as the molar $Mg/(Mg + Fe_{tot})$ with decreasing temperature are positively correlated with decreasing Mg# of the silicate liquid, and increasing degree of crystallization, independent of the initial H_2O content.

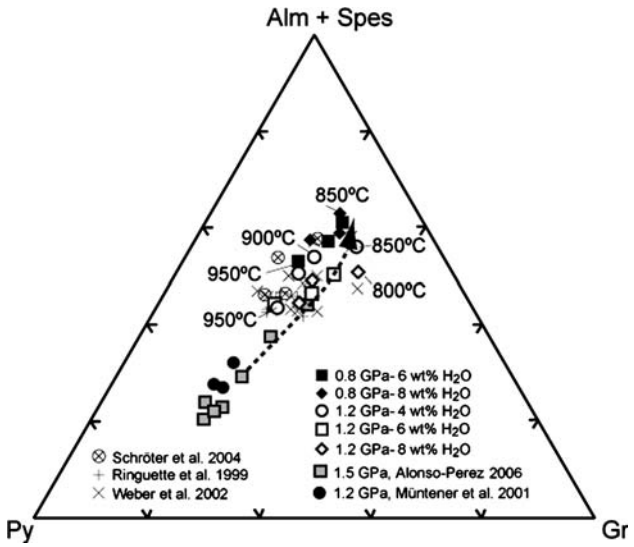

Fig. 4 Experimental garnet composition derived from this study (0.8 and 1.2 GPa) compared to basaltic systems (Alonso-Perez 2006; Müntener et al. 2001) and to natural occurrences from island arc systems (Schroter et al. 2004; Ringuette et al. 1999; Weber et al. 2002). Garnet end-member compositions are calculated based on X-site occupancy (Ca, Fe^{2+}, Mn, Mg). Note the shift towards the almandine-spessartine join for low-pressure (0.8 GPa) garnets (*full symbols*) with respect to the high-pressure (1.2 GPa) garnets (*open symbols*). *Arrow* indicates evolution of garnet compositions during isobaric cooling of the Jijal complex, Kohistan island arc (Müntener et al., unpublished data)

Amphibole

Low-pressure amphiboles at 8 wt% H_2O vary from pargasite to Tschermakitic-hornblende (Leake 1978) with decreasing temperature from 950 to 800°C. The Mg# of amphibole decreases from 0.57 to 0.37 and shows a positive correlation with temperature for variable H_2O contents (Fig. 5a). However, with the substantial increase of Fe–Ti oxide crystallization in experiments at 800°C the Mg# remains approximately constant. Thus, coexisting minerals have an important control on the Mg# of amphibole. In low-pressure experiments with 4 wt% dissolved H_2O, garnet is absent and amphibole coexists with plagioclase and minor amounts of Fe–Ti-oxides, while at higher H_2O contents, garnet is the major coexisting Fe–Mg phase. This is reflected by the intermediate position of the 4 wt% H_2O line, between those of 8 and 6 wt% H_2O, respectively (Fig. 5b). The much higher modal abundance of garnet at 8 wt% H_2O at 0.8 GPa (3.8–10 wt%) as opposed to very small amounts (0.1–1.3 wt%) at 6 wt%, coupled with the low degree of crystallization shifts amphiboles from the 8 wt% H_2O experiments to much higher Mg# because considerable amounts of Fe is accommodated in garnet that exhibits rather low Mg# of 0.2–0.3 (Table 3).

High-pressure amphiboles are ferroan-pargasite at 8 and 6 wt% H_2O and Tschermakite at 4 wt% H_2O and 850°C. The amphibole Mg# decreases from 0.60 to 0.45 with decreasing temperature from 950 to 850°C and H_2O contents from 8 to 4 wt% (Fig. 5a). Thus, at low and high-pressure conditions a systematic decrease of Mg# with temperature is observed. This is illustrated in Fig. 5b, where amphibole and coexisting liquid Mg# are plotted together with data from the literature. The Fe–Mg exchange $\left(K_d^{\sum Fe/Mg}\right)$ between amphibole and liquid derived from this study range between 0.29 and 0.47 and with an average value of 0.38 ± 0.04 Fig. 5b), in agreement with Sisson and Grove (1993a). Moreover, no

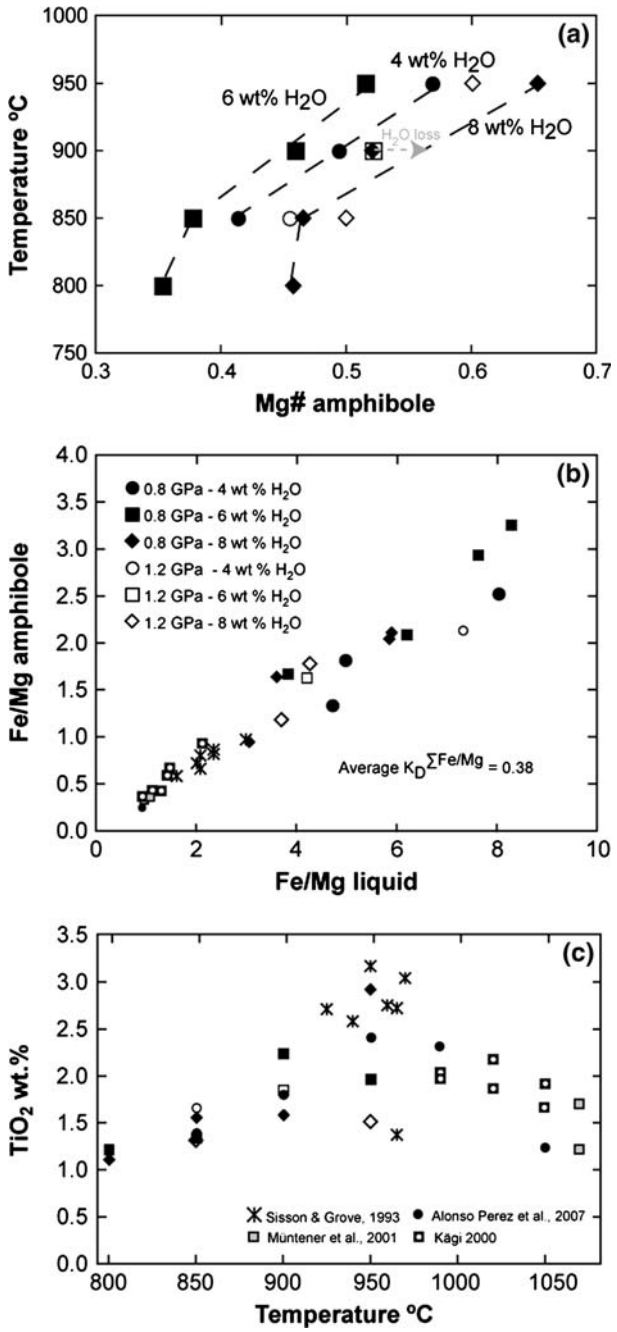

Fig. 5 Amphibole Mg# variations as a function of temperature (**a**), Fe–Mg exchange ($K_d^{\sum Fe/Mg}$) between amphibole and liquid (**b**), and TiO_2 wt% versus temperature for experimental amphiboles (**c**). ($K_d^{\sum Fe/Mg}$) values range between 0.29 and 0.47 with an average value of 0.38 ± 0.04, in agreement with Sisson and Grove (1993a). *Lines* in **a** indicate smooth trends for all experiments except for those with substantial Fe–Ti oxide crystallization at 800°C. Note the shift of the Mg# at 8 wt% H_2O and 900°C close to the 4 wt% H_2O line (rp43) consistent with some water loss

systematic correlation with pressure and a slight decrease in the $K_d^{\sum Fe/Mg}$ with decreasing temperature can be observed. A positive correlation of increasing TiO_2 contents with increasing temperature (Fig. 5c) can be monitored in andesitic bulk compositions up to 950°C, similar to previous studies on TiO_2 in amphibole (Otten 1984; Sisson and Grove 1993a). However, at higher temperatures in basaltic systems the TiO_2 content slightly decreases with increasing temperature indicating incompatible behavior of Ti in the absence of coexisting Fe–Ti-oxides. The Al–Si exchange coefficient ($K_d^{Al/Si}$) between amphibole and liquids is plotted against temperature (Fig. 6) together with experimental amphibole/glass pairs from H_2O saturated low-to intermediate pressure experiments (0.2 GPa) (Sisson and Grove 1993a; Sisson et al. 2005) and from H_2O undersatured experiments on basaltic to andesitic systems Müntener et al. 2001; Kägi 2000). Although a temperature dependence of the $K_d^{Al/Si}$ between amphibole and liquid is apparent, the data suggest that the $K_d^{Al/Si}$ is also pressure and/or composition dependent. Contour lines for high pressure experiments of a given composition show generally higher ($K_d^{Al/Si}$) at a given temperature, than for low pressure experiments.

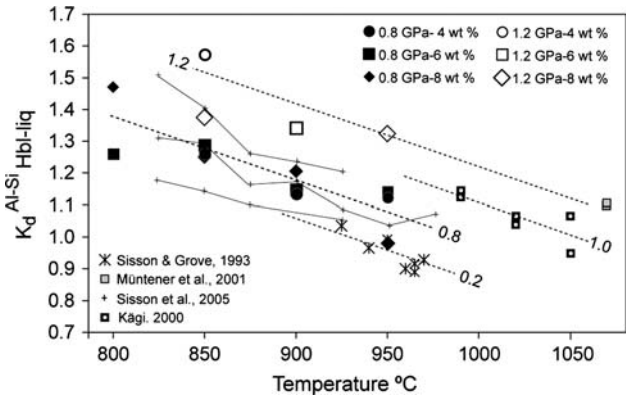

Fig. 6 Molar Al–Si exchange ($K_d^{Al/Si}$) between experimental amphiboles and liquids versus temperature. *Dashed lines* are eye-ball fits to different experimental series at different pressures. *Solid lines* connect experiments on three different compositions at 0.7 GPa and fO_2 similar to our study (Sisson et al. 2005). Positive pressure dependence for a given composition can be observed. High-pressure amphiboles of this study show a higher K_d^{Al-Si} ratio (1.2 GPa, $K_d = 1.4$) than the lower-pressure (0.8 GPa, $K_d = 1.2$) and the 0.2 GPa hydrous experiments ($K_d = 0.94$) of Sisson and Grove (1993a). However, experiments on 3 different compositions at a given pressure and fO_2 similar to this study (QFM and BN experiments of Sisson et al. 2005) indicate that the K_d is also strongly composition dependent

Plagioclase

The variation of the exchange K_d^{Ca-Na} between plagioclase and liquid as a function of liquid H_2O content is illustrated in Fig. 7. The anorthite content of plagioclase is uniformly high for the low pressure experimental series (X_{An} ranging from 0.8 to 0.88, Table 3) and the K_d's vary between 3.5

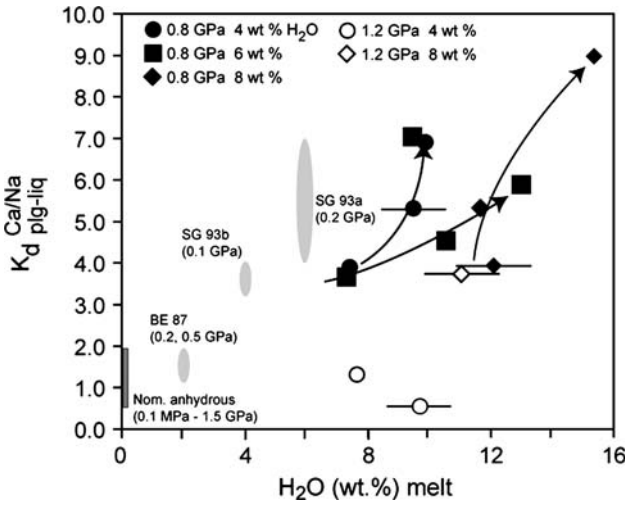

Fig. 7 H_2O contents of andesite liquids determined by Raman spectroscopy (Table 2) versus Ca/Na partitioning between plagioclase and liquid ($K_d^{Ca/Na_{plg-liq}}$). *Arrows* indicate evolution of K_d at a given initial H_2O content with decreasing temperature. *Error bars* indicate ±1 wt% error on the absolute H_2O content, as determined by Raman spectroscopy. *Shaded fields* indicate variations of K_d in H_2O saturated and undersaturated experiments at low pressures: SG93a, 0.2 GPa: Sisson and Grove (1993a), SG93b, 0.1 GPa: (Sisson and Grove 1993b) BE87, (Baker and Eggler 1987). K_d's from nominally anhydrous experiments from 0.01 MPa to 1.5 GPa range from 0.5 to ~2 (data from Baker and Eggler 1987; Bartels et al. 1991; Kinzler and Grove 1992; Draper and Johnston 1992; Villiger et al. 2004)

and 9. In a series of 0.2 GPa H_2O-saturated experiments, it was shown that the exchange K_d progressively increases with melt H_2O content (Sisson and Grove 1993a). However, our results show that the K_d's do not linearly increase at H_2O undersaturated conditions. For each bulk H_2O content, there is a positive correlation of the exchange K_d with liquid H_2O, much like the results from Yoder (1968). Hence, other parameters, such as partitioning of Na between plagioclase and coexisting amphibole ($Ca/Na_{amp} < Ca/Na_{plg}$) are probably responsible for the further increase in K_d^{Ca-Na} with decreasing temperature and hence increasing H_2O content in the melt. The exchange K_d of most of our experiments is substantially higher than in nominally anhydrous experiments between 0.1 MPa and 1.5 GPa (Fig. 7).

Clinopyroxene

Clinopyroxene was only observed in three experiments at 1.2 GPa, 950 and 900°C, and at relatively low liquid H_2O contents between 6 and 4 wt%. The clinopyroxene is high Al_2O_3 diopside (7.6–9.2 wt%). Mg# and Ca-Tschermak's component range between 0.5 and 0.6, and 0.08 and 0.14, respectively.

Oxides

In all but three experiments containing Fe–Ti-oxides, the oxide phase is ilmenite with an average composition of 41.0 wt% TiO_2, and 48.3 wt% FeO (all Fe as Fe^{2+}). The MgO content decreases from 3.3 wt% at 950°C to about 1 wt% at 800°C suggesting a temperature dependent incorporation of Mg into the ilmenite structure. Experiments rp67, rp14 and rp15 (0.8 GPa, 4wt% H_2O, and 1,000–900°C, respectively) contain hercynitic spinel with Mg# ranging from 0.41 to 0.2.

Melt compositions

To evaluate the effects of different solid assemblages on the compositional evolution of experimental liquids during differentiation, we separately evaluate the low- and high-pressure experimental series. Silica increases progressively with increasing differentiation (Fig. 8) from andesitic to dacitic and rhyolitic compositions (TAS diagram, Le Bas et al. 1986). Mg-# of derivative liquids systematically decreases from 0.41 to 0.17 with decreasing temperature from 1,000 to 800°C (Fig. 9). In general, high-pressure derivative liquids have higher Mg# at a given temperature than low-pressure ones. The variability of four major elements (wt%, on a volatile-free base) as a function of the Mg# are illustrated in Fig. 9: SiO_2 and K_2O increase from 56.4 to 76.5 wt% and from 1.4 to 2.8 wt%, respectively, whereas CaO and TiO_2 decreases from 7.2 to 2.9 wt% and from 0.94 to 0.13 wt%,

The quenched glass compositions at 0.8 and 1.2 GPa are simplified by recasting liquid compositions into mineral

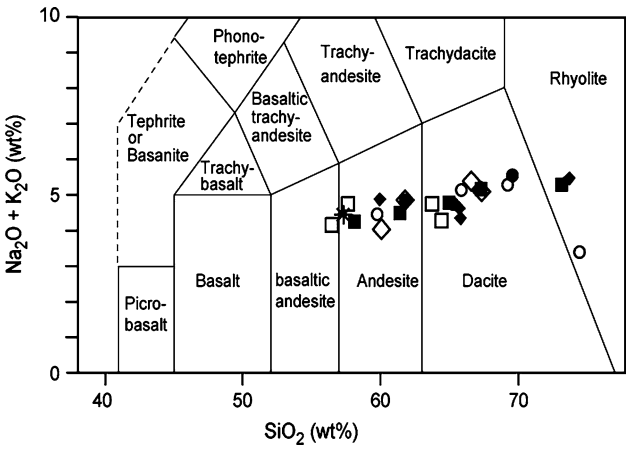

Fig. 8 A portion of the total alkali ($Na_2O + K_2O$) vs silica (SiO_2) diagram (TAS, Le Bas et al. 1986), illustrating the compositional evolution of experimental liquids, recalculated on an anhydrous basis. Derivative liquids cover the range of basaltic andesite–andesite–dacite–rhyolite

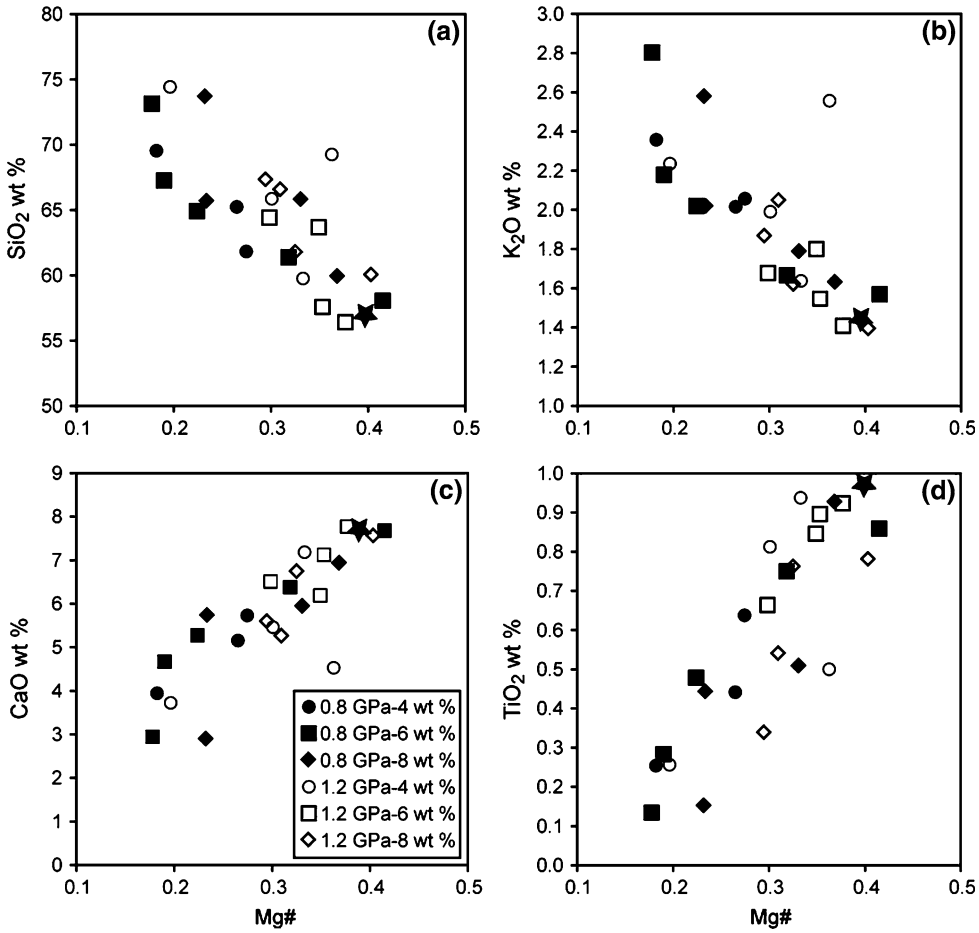

Fig. 9 Derivative liquid major element compositions versus Mg#. SiO_2 (**a**) and K_2O (**b**) increase, whereas CaO (**c**) and TiO_2 (**d**) decrease, with decreasing Mg#

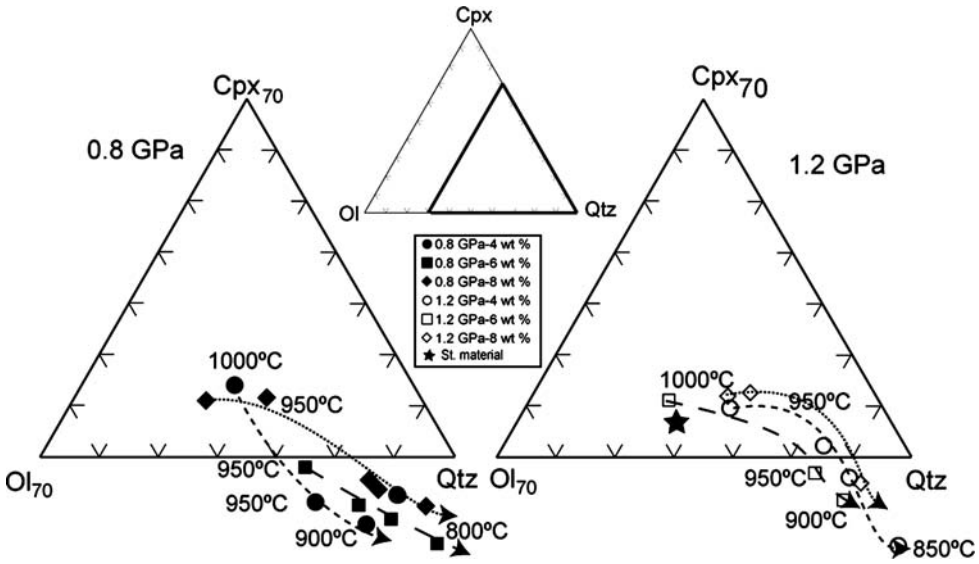

Fig. 10 *Liquid lines* of descent at 0.8 and 1.2 GPa projected into the Olivine–Cpx–Quartz pseudoternary system after Grove et al. (1992). The quenched glass compositions were recalculated into mineral end-member components and projected from spinel, plagioclase and K-feldspar onto the Ol–Cpx–Qtz plane of the basalt tetrahedron. Note that most of the derivative compositions are peraluminous (corundum-normative), a feature that has often been cited as evidence for crustal melting (Conrad et al. 1988)

components and projecting them into the pseudo-ternary olivine–cpx–quartz system of the basalt tetrahedron (Fig. 10). The diagrams are projections through plagioclase and spinel (Grove et al. 1992). All derivative liquids produced in this study are qtz-normative. At 0.8 GPa (Fig. 10a), liquids evolve to per-aluminous compositions mainly because of amphibole- dominated crystalline assemblages, except at the highest temperature (≥950°C) close to the liquidus, and hence close to the original meta-aluminous starting andesite composition. Liquid evolution

is similar at 1.2 GPa (Fig. 10b), with a change from meta-aluminous to peraluminous compositions between 950 and 900°C; higher modal proportions of garnet only slightly retards the evolution to peraluminous compositions. The overall liquid evolution is dominated by amphibole extraction that plots towards the left-side of the ol–cpx–qtz ternary, outside the triangle at positive olivine and cpx and negative Qtz coordinates (nepheline normative), driving residual liquids toward the lower-right corner into the corundum-normative field.

Discussion

Garnet and amphibole phase relations at pressures relevant for arc lower crust

In this study we have explored the roles of H_2O and pressure at lower crustal conditions on the stability of the most important phases in a hydrous andesite liquid that was derived by fractional crystallization at 1.0 GPa from a precursor picrobasaltic mantle-derived liquid. The principal phases we found are garnet, amphibole, clinopyroxene and plagioclase. We have identified rather larger stability fields of garnet at 1.2 GPa and still had small amounts of almandine-rich garnet stable at 0.8 GPa. Garnet stability is clearly linked to the H_2O-content in the silicate liquid: At 0.8 GPa the modal amounts of garnet increase with increasing H_2O contents. The modal amount of garnet decreases with decreasing temperatures at the expense of increasing amphibole and plagioclase implying a reaction relation of the type garnet + $liquid_1$ = amph + plg + $liquid_2$. At 1.2 GPa the situation is somewhat different, as garnet reaches considerably larger maximal modal amounts, coexisting with cpx, at both 4 and 6 wt% initial H_2O content, just at the onset of amphibole crystallization and rapidly decreases thereafter, indicating a peritectic relationship of the type: garnet + cpx + liquid = amphibole. At 8 wt% H_2O the amount of amphibole at higher temperature is considerably larger and, as a consequence, the amount of garnet is reduced. A prime result of this study is that garnet is an igneous phase in typical hydrous, arc-tholeiitic to calc-alkaline derivative liquids at conditions corresponding to a magma reservoir located in the lower crust or at the crust-mantle boundary in convergent-plate margin settings (25–40 km) and hence, its presence as a fractionating phase affecting both major and trace element contents of derivative liquids cannot a priori be attributed to partial melting of (solid) crustal source rocks and/or to melting of the subducting slab.

Estimated crustal thickness in active continental margin settings, range from approximately 70 km in the Andes, to 45 km in western North America, to 30–35 in Alaska (Gill 1981). The phase relationships established at 0.8 and 1.2 GPa, corresponding to a depth of approximately 25–40 km, are thus applicable to magmatic processes at conditions of a mature island arc setting or typical for active continental margin, and correspond to deep-crustal conditions or the crust-mantle boundary. The well-exposed crust-mantle section of the Jijal complex (Kohistan arc, Northern Pakistan) is composed of ultramafic olivine and cpx-rich cumulates (dunite, pyroxenite) at its base, overlain by amphibole and garnet-rich ultramafic rocks [garnet-hornblende pyroxenites, (cpx-) garnet-hornblendites and cpx- and amphibole-bearing garnetites] which in turn are overlain by garnet gabbros (Jan and Howie 1981; Ringuette et al. 1999). In the light of our new results the lithological succession of the upper part of the Jijal complex (starting with garnet and amphibole-rich ultramafic rocks) can be interpreted as fractionated products along a liquid line of decent of a hydrous basaltic andesite to andesite liquids at pressures between 0.8 and 1.2 GPa, temperatures in the range of 800–1,000°C, H_2O contents of 4–8 wt%. Prograde dehydration melting is thus not required to explain arc root rock sequences (cf. Yoshino and Okudaira 2004; Garrido et al. 2006).

Phase control on meta-aluminous and peraluminous derivative liquids

Regarding the composition of our derivative liquids, there are two principal results: (1) the vast majority of our andesitic to rhyolitic liquids are peraluminous (corundum-normative, negative cpx-component). Peraluminous liquids containing garnet with less than 4 wt% CaO have often been attributed to partial melting of sedimentary (pelitic) sources (Chappell et al. 1987; Conrad et al. 1988). However, such peraluminous granitoid rocks ranging from qtz-diorites to leucogranites are widespread in batholitic complexes (Ulmer et al. 1983; Blundy and Sparks 1992). Various experimental studies performed at our laboratory (Kägi 2000; Müntener and Ulmer 2006; Ulmer 2007 and unpublished data) in the range 0.5–1.5 GPa on both equilibrium and fractional crystallization, and literature data at various pressures (Sisson and Grove 1993a; Müntener et al. 2001) indicate that peraluminous derivative liquids are mainly produced from meta-aluminous parental magmas at a restricted pressure range of about 0.7–1.2 GPa: At higher pressure (Alonso-Perez 2006) garnet precipitation inhibits the evolution towards peraluminous liquids, whereas at lower pressure dominance of An-rich plagioclase in hydrous systems keeps the liquids meta-aluminous. The ‘critical’ pressure range of about 0.7–1.2 GPa is characterized by the dominance of amphibole in the fractionating assemblage that is only initially joined by cpx (at relatively low H_2O-contents)

and the delay of plagioclase crystallization. This is in line with the original proposal by Cawthorn and Brown (1976) that identified amphibole as the dominant phase controlling the formation of corundum-normative liquids from meta-aluminous liquids. In summary, our phase equilibria clearly show that while garnet could crystallize from meta-aluminous andesite liquids under favorable conditions (high-pressure, high H_2O-contents) and will strongly control some trace elements in the derivative liquids (e.g. Sr, Y, HREE), amphibole is the dominant phase controlling the major element characteristic of these magmas (high SiO_2, peraluminous).

A second order effect related to amphibole fractionation is the observed Al/Si partitioning behavior between amphibole and liquid (Fig. 6): With increasing pressure, the $K_d^{Al/Si}((A1/Si)_{amph}/(Al/Si)_{liq})$ increases and becomes larger than unity at 0.8 GPa. Therefore, it is probably not only garnet that drives derivative liquids at high pressure to meta-aluminous compositions (see above) but also amphibole becomes less efficient in crossing the peraluminous meta-aluminous compositional divide. However, given the large variability of $K_d^{Al/Si}((A1/Si)_{amph}/(Al/Si)_{liq})$ for different compositions at a given pressure (Fig. 6), these statements must remain qualitative at this point.

Calc-alkaline differentiation at high pressure?

The general evolution of derivative liquids in terms of tholeiitic versus calc-alkaline differentiation trends is illustrated in a binary FeO*/MgO versus SiO_2 wt% diagram (Fig. 11), (Miyashiro 1974) together with the fO_2 fields established by Sisson et al. (2005). High-pressure liquids remain in the calc-alkaline field, whereas low-pressure and high water content (6–8 wt% H_2O) liquids show a distinctly tholeiitic evolutionary trend. As shown before, the dominant plagioclase-amphibole crystallization at low-pressure, and high water contents (6–8 wt% H_2O) drives derivative liquids to high SiO_2 contents at moderately high FeO*/MgO values compared to the high-pressure evolutionary trend, where garnet is an abundant phase that is not only silica-poor, but has a rather high $K_d^{Fe-Mg_{solid-liq}}$ that produced high SiO_2 and relatively low FeO*/MgO characteristics of calc-alkaline products. The recent study of Sisson et al. (2005) concluded that in hydrous granite–rhyolite liquids at moderate pressure (0.7 GPa) and an fO_2 ranging from ~QFM to Ni–NiO +1.3 to +4, the amount and composition of evolved liquids and coexisting mineral assemblages vary as functions of fO_2 and temperature, with melt being more evolved at higher fO_2. Furthermore, they argue that the best comparison of natural silicic magmas and experimentally produced liquids could be done in the discriminant diagram for tholeiitic versus calc-alkaline magmas (Miyashiro 1974), contoured for fO_2. This is illustrated in Fig. 11, where we plotted some of the experimental data of Sisson et al. (2005), together with the experiments from this study. Their experiments with a similar setup to our experiments (fO_2 around QFM or BN) closely overlap with our data, while their high fO_2 experiments ($MnO–Mn_3O_4$ buffer: corresponding to QFM +4) plot on the high SiO_2 – low FeO*/MgO part of the diagram (Fig. 11). Data from this study are consistent with their conclusions; however, we point out that for a given fO_2, pressure dependent phase equilibria are an important additional control on derivative granitic liquids.

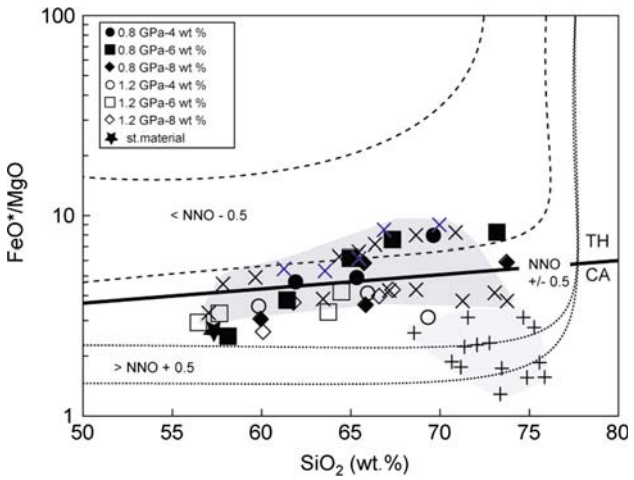

Fig. 11 Compositional characteristics of derivative liquids in an FeO*/MgO versus SiO_2 diagram depicting the calc-alkaline/tholeiitic dividing line from Miyashiro (1974) and fO_2 fields from Sisson et al. (2005) for high-silica liquids. Crosses within light shaded field: highly oxidized experiments (buffered by $MnO–Mn_3O_4$), diagonal crosses within darker shaded field: reduced experiments performed at QFM and BN from Sisson et al. (2005). Note that highly oxidized experiments tend to very low FeO*/MgO ratios

An important effect of garnet, in addition to its influence on the trace element characteristics of derivative liquids, is its influence on the iron–magnesium ratio of derivative liquids. Garnet has a rather high Fe/Mg solid/liquid partitioning coefficient (0.78–0.92 at 0.8–1.5 GPa) and hence tends to produce 'high-Mg' liquids (similar to magnetite) unlike amphibole that has a considerably lower Fe/Mg solid/liquid K_d (0.32–0.45 at 0.8–1.5 GPa), comparable to olivine and pyroxenes, and therefore, extracts Mg more efficiently, leading to lower FeO*/MgO liquids at a given SiO_2-content (compare the high and low pressure series of Fig. 11). Bulk rock data from the plutonics of the Kohistan batholith (Jagoutz et al. submitted; Enggist personal communication 2008) indicates that high Sr/Y granitoid rocks display lower FeO*/MgO at a given SiO_2 than comparable rocks with low Sr/Y ratios, supporting a potential role of garnet in producing "high-Mg# granitoids". We tentatively

propose that some leucogranites do not a priori represent 'crustal melts', but they might be formed directly by crystal fractionation at high pressures.

Absence of garnet leads to derivative liquids with rather high FeO*/MgO contents at a given SiO_2 content, whereas garnet suppresses this trend due to its high Fe/Mg partition coefficient and keeps derivative liquids at rather low FeO*/MgO ratios. At shallow pressure conditions (e.g. <0.5 GPa), fO_2 plays a dominant role by stabilizing Fe–Ti-oxides (magnetite, hercynite, ulvospinel) to higher temperature and thus leading to higher modal amounts of these phases under oxidizing conditions (e.g. Sisson and Grove 1993a; Sisson et al. 2005). It should be mentioned that rather low amounts of Fe–Ti oxide phases in high-pressure cumulates from island arc and active continental margins are a common feature: plagioclase-poor to plagioclase absent pyroxenites and hornblendites in the Jijal section of the Kohistan arc (Jan and Howie 1981; Ringuette et al. 1999; Müntener et al. unpublished data), and pyroxenitic to hornblenditic cumulates from the Adamello, Italy (Blundy and Sparks 1992; Ulmer et al. 1983); usually contain low modal amounts of Fe–Ti phases, unlike shallower gabbroic cumulates that contain abundant magnetite (Ulmer et al. 1983).

Acknowledgments We are grateful to S. Pilet for measuring CO_2 and H_2O in the starting material by FT-IR at Caltech. We thank Bruno Scaillet and Alan Thompson for comments and M.J. Krawczynski who provided a helpful review that improved the paper. Insightful and constructive comments by T.W. Sisson forced us to think harder about CO_2 and fO_2 and substantially improved the overall content of the paper. This research was supported by the Swiss NSF (Grants nr. 2000-61894.00/1).

References

Allen JC, Boettcher AL (1978) Amphiboles in andesite and basalt: II. Stability as a function of P–T-fH_2O-fO_2. Am Mineral 63:1074–1087

Allen JC, Boettcher AL (1983) The stability of amphibole in andesite and basalt at high pressures. Am Mineral 68:307–314

Allen JC, Boettcher AL, Marland G (1975) Amphiboles in andesite and basalt: I. Stability as a function of P–T-fO_2. Am Min 60:1069–1085

Alonso-Perez R (2006) The role of garnet in the evolution of hydrous, calc-alkaline magmas: an experimental study at 0.8–1.5 GPa. PhD thesis, ETH Zurich, p 174

Atherton MP, Petford N (1993) Generation of sodium-rich magmas from newly underplated basaltic crust. Nature 362:144–146. doi:10.1038/362144a0

Baker DR, Eggler DH (1987) Compositions of anhydrous and hydrous melts coexisting with plagioclase, augite, and olivine or low-Ca pyroxene from 1 atm to 8 kbar: application to the Aleutian volcanic center of Atka. Am Min 72:12–28

Bartels KS, Kinzler RJ, Grove TL (1991) High pressure phase relations of primitive high-alumina basalts from Medicine Lake volcano, northern California. Contrib Mineral Petrol 108:253–270. doi:10.1007/BF00285935

Blundy JD, Sparks RSJ (1992) Petrogenesis of mafic inclusions in granitoid magmas of the Adamello massif, Italy. J Petrol 33:1039–1104

Blundy JD, Wood BJ (2003) Partitioning of trace elements between crystals and melts. Earth Planet Sci Lett 210:383–397

Bowen NL (1928) The evolution of igneous rocks. Princeton University Press, NJ

Burg JP, Bodinier JL, Chaudhry S, Hussain S, Dawood H (1998) Infra-arc mantle-crust transition and intra-arc mantle diapirs in the Kohistan complex (Pakistani Himalaya): petro-structural evidence. Terra Nova 10:74–80. doi:10.1046/j.1365-3121.1998.00170.x

Cawthorn RG, Brown PA (1976) A model for the formation and crystallization of corundum-normative calcalkaline magmas through amphibole fractionation. J Geol 84:467–476

Cawthorn RG, O'Hara MJ (1976) Amphibole fractionation in calc-alkaline magma genesis. Am J Sci 276:309–329

Chappell BW, White AJR, Wyborn D (1987) The importance of residual source material (restite) in granite petrogenesis. J Petrol 28(6):1111–1138

Coleman RG, Lee DE, Beatty LB, Brannock WW (1965) Eclogites and eclogites–their differences and similarities. Geol Soc Am Bull 76:483–508. doi:10.1130/0016-7606(1965)76[483:EAETDA]2.0.CO;2

Conrad WK, Nicholls IA, Wall VJ (1988) Water-saturated and -undersaturated melting of metaluminous and peraluminous crustal compositions at 10 kb: evidence for the origin of silicic magmas in the Taupo Volcanic Zone, New Zealand, and other occurrences. J Petrol 29:765–803

Davidson J, Turner S, Handley H, Macpherson C, Dosseto A (2007) Amphibole 'sponge' in the arc crust. Geology 35:787–790. doi:10.1130/G23637A.1

Day RA, Green TH, Smith IEM (1992) The origin and significance of garnet phenocrysts and garnet-bearing xenoliths in miocene calc-alkaline volcanics from Northland, New Zealand. J Petrol 33:125–161

DeBari SM, Coleman RG (1989) Examination of the deep levels of an island arc: Evidence from the Tonsina ultramafic-mafic assemblage, Tonsina, Alaska. J Geophys Res 94:4373–4391. doi:10.1029/JB094iB04p04373

Defant MJ, Drummond MS (1990) Derivation of some modern arc magmas by melting of young subducted lithosphere. Nature 347:662–665. doi:10.1038/347662a0

Di Muro A, Villemant B, Montagnac G, Scaillet B, Reynard B (2006) Quantification of water content and speciation in natural silicic glasses (phonolite, dacite, rhyolite) by confocal micro-Raman spectrometry. Geochim Cosmochim Acta 70:2868–2884. doi:10.1016/j.gca.2006.02.016

Dixon JE, Pan V (1995) Determination of the molar absorptivity of dissolved carbonate in basanitic glass. Am Min 80:1339–1342

Dixon JE, Stolper EM, Holloway JR (1995) An experimental study of water and carbon dioxide solubilities in mid-ocean ridge basaltic liquids 1. Calibration and solubility models. J Petrol 36:1607–1631

Draper DS, Johnston AD (1992) Anhydrous PT phase relations of an aleutian high-MgO basalt: an investigation of the role of olivine-liquid reaction in the generation of high-alumina basalts. Contrib Mineral Petrol 112:501–519. doi:10.1007/BF00310781

Ducea MN, Saleeby JB (1996) Buoyancy sources for a large, unrooted mountain range, the Sierra Nevada, California: evidence form xenolith thermobarometry. J Geophys Res 101(B4):8229–8244. doi:10.1029/95JB03452

Ducea MN, Saleeby JB (1998) The age and origin of a thick mafic-ultramafic keel from beneath the Sierra Nevada batholith. Contrib Mineral Petrol 133:169–185. doi:10.1007/s004100050445

Evans BW, Vance JA (1987) Epidote phenocrysts in dacitic dikes, Boulder county, Colorado. Contrib Mineral Petrol 96:178–185. doi:10.1007/BF00375231

Fitton JG (1972) The genetic significance of almandine-pyrope phenocrysts in the calc-alkaline Borrowdale volcanic group, Northern England. Contrib Mineral Petrol 36:231–248. doi:10.1007/BF00371434

Gaetani GA, Grove TL (1998) The influence of water on melting of mantle peridotite. Contrib Mineral Petrol 131:323–346. doi:10.1007/s004100050396

Garrido CJ, Bodinier J-L, Burg J-P, Zeilinger G, Hussain SS, Dawood H, Chaudry N, Gervilla F (2006) Petrogenesis of mafic garnet granulite in the lower crust of the Kohistan Paleo-arc complex (Northern Pakistan): Implications for intra-crustal differentiation of island arcs and generation of continental crust. J Petrol 47:1872–1914. doi:10.1093/petrology/egl030

Gill JB (1981) Orogenic Andesites and plate tectonics. Springer, Berlin, p 390

Green TH (1972) Crystallization of calc-alkaline andesite under controlled high pressure hydrous conditions. Contrib Mineral Petrol 34:150–166. doi:10.1007/BF00373770

Green TH (1992) Experimental phase equilibrium studies of garnet-bearing I-type volcanics and high-level intrusives from Northland, New Zealand. Trans R Soc Edinb Earth Sci 83:429–438

Green TH, Ringwood AE (1968a) Genesis of the calc-alkaline igneous rock suite. Contrib Mineral Petrol 18:105–162. doi:10.1007/BF00371806

Green TH, Ringwood AE (1968b) Origin of garnet phenocrysts in calc-alkaline rocks. Contrib Mineral Petrol 18:163–174. doi:10.1007/BF00371807

Greene AR, DeBari SM, Kelemen PB, Blusztain J, Clift PD (2006) A detailed geochemical study of island arc crust: the Talkeetna arc section, south-central Alaska. J Petrol 47:1051–1093. doi:10.1093/petrology/egl002

Grove TL, Kinzler RJ, Bryan WB (1992) Fractionation of mid-ocean ridge basalt (MORB). In: Phipps Morgan J, Blackman DK, Sinton JM (eds) Mantle flow and melt generation at mid-ocean ridges, vol 71. American Geophysical Union, Washington, DC, pp 281–310

Hall LJ, Brodie J, Wood BJ, Carroll MR (2004) Iron and water losses from hydrous basalts contained in $Au_{80}Pd_{20}$ capsules at high pressure and temperature. Min Mag (Lond) 68:75–81. doi:10.1180/0026461046810172

Harangi SZ, Downes H, Kosa L, Szabo C, Thirlwall MF, Mason PRD, Mattey DP (2001) Almandine Garnet in calc-alkaline volcanic rocks of the Northern Pannonian basin (Eastern Central Europe): Geochemistry, petrogenesis and geodynamic implications. J Petrol 42:1813–1843. doi:10.1093/petrology/42.10.1813

Helz RT (1982) Phase relations and compositions of amphiboles produced in studies of the melting behavior of rocks. In: Ribbe P (ed) Amphiboles; petrology and experimental phase relations. Mineralogical Society of America, Washington, DC, pp 279–353

Huang W-L, Wyllie PJ (1986) Phase relationships of gabbro-tonalite-granite-water at 15 kbar with applications to differentiation and anatexis. Am Min 71:301–316

Jan MQ, Howie RA (1981) The mineralogy and geochemistry of the metamorphosed basic and ultrabasic rocks of the Jijal complex, Kohistan, NW Pakistan. J Petrol 22:85–126

Kägi R (2000) The liquid line of descent of hydrous, primary calc-alkaline magmas under elevated pressure. An experimental approach. PhD thesis, ETH Zürich, p 100

Kägi R, Müntener O, Ulmer P, Ottolini L (2005) Piston cylinder experiments on H_2O undersaturated Fe-bearing systems: an experimental setup approaching fO_2 conditions of natural calc-alkaline magmas. Am Min 90:708–717. doi:10.2138/am.2005.1663

Kay S, Mahlburg KS, Kay RW (1985) Aleutian tholeiitic and calc-alkaline magma series I: the mafic phenocrysts. Contrib Mineral Petrol 90:276–290. doi:10.1007/BF00378268

Kelemen PB, Hanghøj K, Greene AR (2003) One view of the geochemistry of subduction-related magmatic arcs, with an emphasis on primitive andesite and lower crust. In: Rudnick RL (ed) The crust. Elsevier, New York, pp 593–659

Kinzler RJ, Grove TL (1992) Primary magmas of mid-ocean ridge basalts 1. Experiments and methods. J Geophys Res 97:6885–6906. doi:10.1029/91JB02840

Kress VC, Carmichael ISE (1991) The compressibility of silicate liquids containing Fe2O3 and the effect of composition, temperature, oxygen fugacity and pressure on their redox states. Contrib Mineral Petrol 108:82–92. doi:10.1007/BF00307328

Kushiro I (1987) A petrological model of the mantle wedge and lower crust in the Japanese island arcs. In: Mysen B (ed): Magmatic processes, physicochemical principles. Geochem Soc Spec Publ 1:165–181

Le Bas MJ, Lemaitre RW, Streckeisen A, Zanettin B (1986) A chemical classification diagram of volcanic rocks based on the total alkali silica diagram. J Petrol 27(3):745–750

Leake BE (1978) Nomenclature of amphiboles. Am Min 63:1023–1052

Mercier M, Di Muro A, Giordano D, Métrich N, Lesne P, Pichavant M, Scaillet B, Clocchiatti R, Montagnac G (2008) Influence of glass polymerization and oxidation on Micro-Raman water analysis in alumino-silicate glasses. Geochim Cosmochim Acta (in press)

Miyashiro A (1974) Volcanic rock series in island arcs and active continental margins. Am J Sci 274:321–355

Müntener O, Ulmer P (2006) Experimentally derived high-pressure cumulates from hydrous arc magmas and consequences for the seismic velocity structure of island arc crust. Geophys Res Lett 31:L21308. doi:10.1029/2006GL027629

Müntener O, Kelemen PB, Grove TL (2001) The role of H_2O during crystallization of primitive arc magmas under uppermost mantle conditions and genesis of igneous pyroxenites: an experimental study. Contrib Mineral Petrol 141:643–658

Mysen BO (1988) Structure and properties of silicate melts. Elsevier, Amsterdam

Osborn EF (1959) Role of oxygen pressure in the crystallization and differentiation of basaltic magma. Am J Sci 257:609–647

Newman S, Stolper E, Stern R (2000) H_2O and CO_2 in magmas from the Mariana arc and back arc systems. Geochem Geophys Geosystems 1. doi:10.1029/1999GC000027

Otten MT (1984) The origin of brown hornblende in the Artfjället gabbro and dolerites. Contrib Mineral Petrol 86(2):189–199. doi:10.1007/BF00381846

Pilet S, Baker M, Stolper EM (2008) Metasomatized lithosphere and the origin of alkaline lavas. Science 320:916–919. doi:10.1126/science.1156563

Ratajeski K, Sisson TW (1999) Loss of iron to gold capsules in rock-melting experiments. Am Min 84:1521–1527

Ringuette L, Martignole J, Windley BF (1999) Magmatic crystallization, isobaric cooling, and decompression of the garnet-bearing assemblages of the Jijal sequence (Kohistan terrane, western Himalayas). Geology 27:139–142. doi:10.1130/0091-7613(1999)027<0139:MCICAD>2.3.CO;2

Rudnick RL (1995) Making continental crust. Nature 378:571–577. doi:10.1038/378571a0

Schroter FC, Stevenson JA, Daczko NR, Clarke GL, Pearson NJ, Klepeis KA (2004) Trace element partitioning during high-P partial melting and melt-rock interaction; an example from northern Fiordland, New Zealand. J Metamorph Geol 22(5):443–457. doi:10.1111/j.1525-1314.2004.00525.x

Sisson TW, Grove TL (1993a) Experimental investigations of the role of H_2O in calc-alkaline differentiation and subduction zone

magmatism. Contrib Mineral Petrol 113:143–166. doi:10.1007/BF00283225

Sisson TW, Grove TL (1993b) Temperatures and H_2O contents of low MgO high-alumina basalts. Contrib Mineral Petrol 113:167–184. doi:10.1007/BF00283226

Sisson TW, Ratajeski K, Hankins WB, Glazner AF (2005) Voluminous granitic magmas from common basaltic sources. Contrib Mineral Petrol 148:635–661. doi:10.1007/s00410-004-0632-9

Stern CR, Huang W-L, Wyllie PJ (1975) Basalt-andesite-rhyolite-H_2O crystallization intervals with excess H_2O and H_2O-undersaturated liquidus surfaces to 35 kilobars, with implications for magma genesis. Earth Planet Sci Lett 28:189–196. doi:10.1016/0012-821X(75)90226-5

Taylor SR (1967) The origin and growth of continents. Tectonophysics 4:17–34. doi:10.1016/0040-1951(67)90056-X

Tiepolo M, Vannucci R, Oberti R, Foley S, Bottazzi P, Zanetti A (2000) Nb and Ta incorporation and fractionation in titanian pargasite and kaersutite; crystal-chemical constraints and implications for natural systems. Earth Planet Sci Lett 176:185–201. doi:10.1016/S0012-821X(00)00004-2

Ulmer P (1986) Basische und ultrabasische Gesteine des Adamello (Provinzen Brescia und Trento, Norditalien). PhD thesis Nr. 8105. ETH Zürich

Ulmer P (1989a) High pressure phase equilibria of a calc-alkaline picro-basalt: Implications for the genesis of calc-alkaline magmas. Carnegie Inst Wash Yb 88:28–35

Ulmer P (1989b) Partitioning of High Field Strength Elements among olivine, pyroxenes, garnet and calc-alkaline picrobasalts: experimental results and an application. Carnegie Inst Wash Yb 88:42–47

Ulmer P (2007) Differentiation of mantle-derived calc-alkaline magmas at mid to lower crustal levels: experimental and petrologic constraints. Minerva 76:309–325

Ulmer P, Callegari E, Sonderegger UC (1983) Genesis of the mafic and ultramafic rocks and their genetical relations to the tonalitic-trondhjemitic granitoids of the southern part of the Ademello Batholith, (Northern Italy). Mem Soc Geol Ital 26:171–222

Villiger S, Ulmer P, Müntener O, Thompson AB (2004) The liquid line of descent of anhydrous, mantle-derived, tholeiitic liquids by fractional and equilibrium crystallization—an experimental study at 1.0 GPa. J Petrol 45:2369–2388. doi:10.1093/petrology/egh042

Villiger S, Ulmer P, Müntener O (2007) Equilibrium and fractional crystallization experiments at 0.7 GPa: the effect of pressure on phase relations and liquid compositions of tholeiitic magmas. J Petrol 48:159–184. doi:10.1093/petrology/egl058

Weber MBI, Tarney J, Kempton PD, Kent RW (2002) Crustal make-up of the Northern Andes; evidence based on deep crustal xenolith suites, Mercaderes, SW Colombia. In: Wörner G, Jaillard E (eds) Andean geodynamics. Elsevier, Amsterdam

Wilke M, Behrens H (1999) The dependence of the partitioning of iron and europium between plagioclase and hydrous tonalitic melt on oxygen fugacity. Contrib Mineral Petrol 137:102–114. doi:10.1007/s004100050585

Yoder HS (1968) Albite-anorthite-quartz-water at 5 kbar. Carnegie Inst Wash Yb 66:477–478

Yoshino T, Okudaira T (2004) Crustal growth by magmatic accretion constrained by metamorphic p-T paths and thermal models of the Kohistan arc, NW Himalayas. J Petrol 45:2287–2302. doi:10.1093/petrology/egh056

Zajacz Z, Halter W, Malfait W, Bachmann O, Bodnar RJ, Hirschmann MM, Mandeville CW, Morizet Y, Müntener O, Ulmer P, Webster J (2005) A composition-independent quantitative determination of the water content in silicate glasses and silicate melt inclusions by confocal Raman spectroscopy. Contrib Mineral Petrol 150:631–642. doi:10.1007/s00410-005-0040-9